Angewandte Chemie
Eine Zeitschrift der Gesellschaft Deutscher Chemiker

Supporting Information

Super- and Ferroelastic Organic Semiconductors for Ultraflexible Single-Crystal Electronics

Sang Kyu Park+, Hong Sun+, Hyunjoong Chung, Bijal B. Patel, Fengjiao Zhang, Daniel W. Davies, Toby J. Woods, Kejie Zhao, and Ying Diao**

anie_202004083_sm_miscellaneous_information.pdf
anie_202004083_sm_Checkcif.zip
anie_202004083_sm_Movie_S1.mpeg
anie_202004083_sm_Movie_S2.mpeg
anie_202004083_sm_Movie_S3.mpeg
anie_202004083_sm_Movie_S4.mpeg
anie_202004083_sm_Movie_S5.mpeg
anie_202004083_sm_Movie_S6.mpeg
anie_202004083_sm_Movie_S7.mpeg
anie_202004083_sm_Movie_S8.mpeg

Author Contributions

S.K.P. and Y.D. designed the experiments; H.S. and K.Z. designed simulation works; S.K.P. conducted single crystal morphology characterizations (C-POM, AFM and SEM), Raman spectroscopy (DFT calculation), fabricated and characterized electrical performance of two-channel single crystal device; H.S. conducted AIMD, MD, DFT calculations; H.C. conducted Raman spectroscopy and single crystal X-ray diffraction; B.P. conducted SEM and helped to print conductive electrodes; F.Z. performed SEM; D.D. and T.J.W. conducted single crystal X-ray diffraction; S.K.P., H.S., Y.D., and K.Z. wrote the manuscript. Y.D., and K.Z. directed the project.

Table of contents

Methods pg. 1 – 17

Supporting Text 1-4 pg. 18 – 20

Scheme S1 to S3 pg. 21 – 22

Figs. S1 to S34 pg. 23 – 48

Tables S1 to S8 pg. 49 – 54

Captions for Movies S1 to S8 pg. 55

Captions for Supporting Structures 1 and 2 pg. 56

Methods

Materials

Commercially available 6,13-Bis(triisopropylsilylethynyl)pentacene (TIPS-P, ≥ 99%, HPLC, Sigma-Aldrich), Poly(3,4-ethylenedioxythiophene)-poly(styrenesulfonate) (PEDOT:PSS, dry re-dispersible pellets, Sigma-Aldrich), Poly(4-vinylphenol) (PVP, $M_w = 25000$ g mol^{-1}, Sigma-Aldrich), 4,4'-(hexafluoroisopropylidene)diphthalic anhydride (HDA, 99%, Sigma-Aldrich), propylene glycol monomethyl ether acetate (PGMEA, ≥ 99.5%, Sigma-Aldrich), toluene (anhydrous, 99.8%, Sigma-Aldrich), Poly(vinylidene fluoride-co-hexafluoropropylene) (PVDF, M_w ~ 400,000, Sigma-Aldrich), and 1-ethyl-3-methylimidazolium bis(trifluoromethylsulfonyl) imide ([EMIM][TFSI], Solvionic) have been purchased and used without further purification. Commercially available poly(dimethylsiloxane) (PDMS, Sylgard 184, Dow Corning) and polyethylene terephthalate (PET, 0.33 and 0.50 mm in thickness) have been employed as deformable substrates.

Methods

(Thermo-)Mechanical Test Specimens Fabrication:

We have prepared TIPS-P single crystals based on recrystallization method (ca. 20 mg ml^{-1} in ethyl acetate). Single crystals with length range from a few hundred micrometers to several millimeters have been collected by filtration and dried in an ambient condition for few days. Using TIPS-P crystals of single domain, (thermo-)mechanically-induced phase transformation, single crystal structure, and mechano-electrical characteristics (in a two-terminal configuration) are investigated, *vide infra*.

To examine (thermo-)mechanically induced cooperative structural transitions, we adopt freestanding jumping board configuration as illustrated in **Scheme S1a**. We attach a microscope cover glass onto a SiO_2/Si base substrate, then about half of the TIPS-pentacene crystal is placed onto the cover glass, which is fixed using small amount of epoxy glue so that another half of the crystal becomes floated to give freestanding region.

We have also employed ionic gel as a crystal shearing experimental platform due to the fact that 1) ionic liquid does not dissolve TIPS-P at a high temperature condition and 2) liquid-like behavior at a range of high temperature to afford quasi-freestanding feature to the partially glued single crystal onto it (see **Scheme S1b**). To introduce ionic gel onto the target substrates, solution of 1:9:8 PVDF:[EMIM][TFSI]:acetone blend in weight is spin-coated (2000 rpm, 60 s) after plasma treatment of target substrates for 360 seconds at 150 W (PDC-001, Harrick Plasma).

In addition to abovementioned sample with (quasi-)freestanding configurations, we have investigated ferroelastic transition behaviors upon bending or stretching the crystals. For this, the crystals are placed on PDMS and PET substrates and fixed both ends with epoxy glue (see **Scheme S1c**).

Device Fabrication:

To investigate the mechano-electrical characteristics of TIPS-P single crystals upon tensile bending condition, we have constructed a two-terminal configuration device on a PET substrate. The PET substrates are cleaned with toluene, acetone, and isopropyl alcohol, followed by plasma treatment (360 s, at 150W). To introduce a surface passivation layer on the precleaned PET substrates, thin polymer film of cross-linked PVP:HDA (10:1 by weight) is deposited by spin-coating (4500 rpm, 60 sec), using a 5 mg ml^{-1} PVP:HDA blend solution in PGMEA. After spin-coating procedure, the substrates are annealed at 80°C for an hour. The passivation layer enhances both adhesion of single crystal and wettability of PEDOT:PSS ink. Recrystallized TIPS-P crystals are electrostatically adhered on top of the substrates, followed by solution printing of deformable PEDOT:PSS electrodes based on custom-built pressure-driven 3D printer setup. As a ink, we have formulated 1.3 wt% PEDOT:PSS solution in deionized water: IPA (6:4, v:v). Printing is performed using a stainless-steel nozzle (inner diameter of 0.20 mm, Nordson EFD) connected to a plastic syringe, and set the nozzle tip location at about 50 μm above the substrates. The pressure applied to the syringe is 30 kPa controlled by a high precision fluid dispenser (Ultimus V, Nordson EFD). The printing speed is set to be 50 mm min^{-1} and the base temperature is 60°C, see **Scheme S2**.

Device Characterization:

Characterizations of two-terminal single crystal devices are carried out in ambient condition using a Keysight B1500A semiconductor parameter analyzer (Keysight Technologies). Tensile bending strain is applied to the device using a custom-built bending stage based on a motorized as well as manual linear stage. The strain is estimated by: $\varepsilon = \frac{t_{sub}}{2r}$, where t_{sub} is substrate thickness, and r is radius of curvature. Bending radius in each state is measured by side-view image of the device upon tensile bending condition (**Scheme S3** – side view and strain versus radius plot).

Polarized Optical Microscopy:

A Nikon Eclipse Ci-POL optical microscope equipped with a high-speed camera (Infinity 1, Lumenera Corp.) has been used for (in-situ) polarized optical microscopy experiments. To investigate superelastic transition behaviors of TIPS-P, single crystals based on freestanding jumping board configuration (**Scheme S1a**) are heated (20°C min^{-1}) and sheared with a micromanipulator probe tip on a LTS420 heating stage (Linkam Scientific). As shown in **Movies S2** and **S3**, the electrostatic interaction driven [$\bar{1}$00]-shearing is observed as the probe tip approaches to the crystal, leading to the stable to metastable phase transition for both SE1 and SE2 cases.

Mechanically induced deformation twinning based on FE1 is investigated using single crystals based on quasi-freestanding configuration in **Scheme S1b**. The crystals are sheared along [100]-direction using a micromanipulator probe tip, either at Form I(b) or II stabilizing temperature controlled by the LTS420 heating stage (**Fig. 3b**, **Movies S4**, **S5**). Shape recovery by mechanically induced detwinning is accomplished by loading [$\bar{1}$00]-shear.

Mechanically induced deformation twinning based on FE2 is examined based on single crystals adhered on deformable substrates (**Scheme S1c**). The TIPS-P crystals on deformable substrates (PET and PDMS) are either bent (**Fig. 4b**, **Movie S7**) or stretched (**Fig. S19**) using a custom-built bending or stretching stage, under the microscope. Shape recovery by mechanically induced detwinning is accomplished through releasing tensile stress applied to the deformable substrates.

Raman Spectroscopy:

A Horiba Raman confocal imaging microscope (LabRAM HR 3D) with 785-nm and 832-nm laser excitation sources (50x long working distance objective lens) is employed to obtain (polarized) in-situ Raman spectra of TIPS-P single crystals. All the Raman spectra are obtained using a 300 g mm^{-1} grating, an optical density filter of OD = 0.03, and an exposure time of 15 s.

Temperature-dependent Raman spectra are acquired (at every 10°C, 30 – 220°C, heating rate of 10°C min^{-1}) using a single crystal with freestanding jumping board configuration (**Scheme S1a**). Temperature of the samples is controlled with a Linkam THMS600 stage. To induce superelastic transitions under Raman microscope suit, in-situ $[\bar{1}00]$-shearing has been carried out using a micromanipulator probe tip at 150°C and 210°C for SE1 and SE2, respectively.

Polarized Raman spectra of both pristine and twinned domains based on FE1 and FE2 are taken to identify molecular orientation of TIPS-P in each domain region.[43] For polarized Raman spectra acquisition, half-wave plates are employed to give a rotated polarized laser excitation (acquired spectra at every 10° for total 360° rotation). Pentacene core alignment respect to the crystal morphology is determined by monitoring ratio between Raman peaks for C–C stretching of pentacene core along molecular long-axis (1571 cm^{-1}) and short-axis (1369 cm^{-1}), i.e., I_{1571} / I_{1369} in **Fig. 3c** and **4c**. This ratio is particularly useful for identifying pentacene core orientation because it is self-normalized, even though out-of-plane tilted TIPS-P molecule affords slight nonorthogonal features between these peaks.

Single Crystal X-ray Diffraction:

The single crystal structure of Form III phase of TIPS-P is solved using the diffraction patterns collected at NSF's ChemMatCARS (Sector 15) of the Advanced Photon Source, Argonne National Laboratory. Blue slab crystal is mounted on a 5 μm diameter glass fiber tip with epoxy and is heated up to 169°C with an open-stream Leister heater. The beam energy is 30keV (0.41328Å) and the beam size at the sample is 0.15 × 0.15 mm^2. Data have been collected using Huber 3 circles diffractometer with kappa angle offset 60° and equipped with Pilatus3X 1M (CdTe) detector. The distance between the detector and the crystal is 130 mm. A total of 720 frames have been collected at two θ-angles sitting at 0° and ω-angles sitting at -180°, followed up by two different Kappa = 0° and Kappa = 15°, respectively. The data are collected with the φ-angle scanned over the range of 360° using shutterless mode. A user-friendly data collection software is used. Tiff frames are converted to Bruker sfrm format. Data integration are performed with APEX II suite software. The reduction of data is conducted with SAINT v.8.32B and SADABS v.2013 programs included in the APEX suite. The structure solution and refinement are carried out with SHELX software using the XPREP utility for the space group determination, and the XT and XL programs for the structure solution and refinement, respectively. In the case of the Form III structure, the structures for conjugated-backbone core has been preliminarily resolved, neglecting the spatial resolution of hydrogen atoms constituting TIPS group (cif file is available as *Supporting Structure 1, CCDC 1991343*). This is due to the completely disordered state of the rotator side-chain part, at the experimental condition of 169°C. Besides, the structure after twinning transformation is confirmed based on the abovementioned method (*Supporting Structure 2, CCDC 1991344*). The temperature is set to be ambient condition for this case. Deposition numbers ccdc 1991343 and 1991344 contain the supplementary crystallographic data for this pater. These data are provided free of charge by the joint Cambridge Crystallographic Data Centre and Fachinformationszentrum Karlsruhe Access Structures service www.ccdc.cam.ac.uk/structures.

Diffraction data of a twinned crystal were collected on a Bruker D8 Venture equipped with a four-circle kappa diffractometer and Photon 2 detector. The Iμs microfocus Mo ($\lambda = 0.71073$ Å) source supplied the multi-mirror mono-chromated incident beam. Data were collected as a series of φ scans at 300K. Based on the collected data, the facets of pristine and twinned domains were indexed using APEX3, Bruker (2018). Employing *Cell Now* (Sheldrick, 2008), the orientational relationship between the pristine and twinned domains were analyzed.

Morphology Characterization:

The morphology changes after FE1 and FE2 transformations are characterized using an atomic force microscope (Asylum Research Cypher, Asylum Research) with tapping mode, and a scanning electron microscope (Hitachi S-4800, Hitachi High-Technology Corp.). The active layer thickness of single crystal device is measured using a surface profilometer (Sloan Dektak3ST, Veeco).

Theoretical Quantum-Chemical Calculation:

Molecular geometry of TIPS-P at the ground state and the Raman spectrum thereof are calculated by density functional theory method (DFT). Both geometry optimization and vibrational frequency spectrum are calculated using the B3LYP functional and 6-311g(d) basis set as implemented in Gaussian 09 software.[46] The vibrational scaling factor (0.966) is applied to better match the experimentally observed Raman spectra.

Simulation Methods

Structure Search:

Starting from the given initial configuration, it will be a great challenge to capture the lattice evolution of six degrees of freedom (a, b, c, α, β, and γ) merely by ab-initio modeling at small scale. The automated, iterative algorithms, as described in **Fig. S30**, are proposed to search the stable polymorphs and investigate the single molecular kinetics during the phase transitions induced by heating or mechanical loads. During heating (left panel in **Fig. S30**), Form I is heated up to a temperature range of 127~277°C under NVT ensemble. The structure at elevated temperature is energetically relaxed to reach local energy minima. The first screening will be based on the change in γ, which indicates the major difference between the two polymorphs. The evolved structures with a γ change of 10° (15°) will be selected as the seed Form II (III). Next, other lattice parameters, α, β, a, and b, will be carefully compared using the two inequities as the second screening criterion. The structural search succeeds if two screening criteria are satisfied. Any failure in convergence will lead to a change of setting in parametric input of the heating modeling, such as the heating rate, time step, heating algorithm, etc. The mechanical load follows a similar manner (right panel in **Fig. S30**). The mechanical load is applied by choosing a 3×3 transformation matrix and an initial strain rate of 0.1%. The deformed lattice after each incremental strain will be subject to static relaxation to reach the local energy minimum. The successive screening criteria are the same with those in heating. Different from heating, the lattice will exhibit much more varieties in lattice parameters under different types and different degrees of mechanical load. The structural search during mechanical load usually requires multiple iterative refinement of parametric input to reach the desired final structure. **Table S5** demonstrates the lattice parameters of three polymorphs obtained from structural searching under heating or different types of mechanical loads, which match well with the experimental data. During heating, the thermal energy causes both rotational and displacive motions of the backbone in Form I. In the further energetic optimization of the molecule configuration at the saddle point, Form II emerges with the characteristics of γ being reduced by 11.9° and b axis being increased by 0.7 Å. Three different strain matrixes, including the pure shear ε_{xy}, uniaxial tension ε_y and tri-axial tension, enable the lattice transition from Form I to Form II. Among them, the pure shear ε_{xy} requires the lowest threshold strain (8.5%) to yield the lattice of Form II. Besides, Form III could also be obtained by applying appropriate shear strain (a combination of two shear strain matrixes) onto Form I. The generated Form II and Form III from the mother lattice of Form I will be adopted as the initial structure input for the following large scale atomic simulation. All the calculations in the Structure Search part are done by the Vienna Ab-initio Simulation Package (VASP),[47] in which the projector-augmented wave pseudopotentials and the general gradient approximation for the exchange-correlation functional are used. The general dispersion correction (DFT-D3 method)[48] for the GGA-PBE functional[49] is added to accurately mimic the inter-molecular interactions in the molecular crystal. The plane-wave set is expanded within an energy cutoff of 520 eV and the 2×2×1 mesh of k points in the Monkhorst-Pack scheme is chosen for the Brillouin zone sampling. The geometric optimization is considered complete when the magnitude of force per atom is smaller than 0.02 eV/Å. In the heating searching, the temperature of the ab-initio molecular dynamics is controlled by the Nosé–Hoover thermostat with a timestep of 0.1fs.

Ab-initio Modeling (AIMD):

The superelastic transition is investigated by applying the DFT simulation onto the 2×2×1 supercell. The supercell model, containing 400 atoms (four molecules), is built by expanding the optimized unit cell obtained from the Structure Searching part. The calculations are carried out based on the hybrid Gaussian and plane waves scheme implemented in the CP2K package.[50] The DZVP molecularly optimized basis sets and a 400 Ry cutoff auxiliary plane-wave basis set are employed,[51,52] with accompanying Goedecker–Teter–Hutter pseudopotentials.[53] The exchange and correlation term is treated by the PBE functional with the DFT-D3 correction.[48,49] The shear-induced superelastic transition I from Form II to Form I at 127°C (SE1) and superelastic transition II from Form III to Form II at 227°C (SE2) are accomplished by the ab-initio Molecular Dynamics (AIMD) simulation with the aid of the quasi-static loading algorithm. Basically, we apply incremental 1% shear strain ε_{xy} onto the supercell model at each step, and afterward, the model undergoes the ab-initio molecular dynamics in the canonical ensemble NVT for 2 ps at each strained state. After that, the lattice structure of a new phase obtained from the dynamic transition will be fully relaxed and optimized until the atomic displacements are lower than 1.6×10^{-4} nm and forces on the atoms are smaller than 0.23 eV/nm. The recovery process of the superelastic transition is conducted by applying the reverse shear strain of -1% at each step followed by the successive ab-initio molecular dynamics in a similar manner as that of the loading process. The lattice parameters of all polymorphs calculated in the cyclic shear loading have an excellent comparison with the experimental measurements shown in **Table S1**. The temperature is controlled using the generalized langevin thermostat with the time step of 0.5 fs and all periodic boundary conditions are adopted in the DFT simulation. The stress-strain curves of SE1 and SE2 in **Fig. S10** show the characteristics of the superelastic behavior with the small hysteresis. The calculations are done by applying the 0.2% incremental shear strain onto the 2×2×1 supercell model at each step followed by the static geometric optimization. The unloading recovery is conducted by applying the reverse shear strain of -0.2% at each step up to the corresponding stress is reduced to zero.

Molecular Dynamics:

The large-scale molecular dynamics is employed to investigate the ferroelasticity. The simulation is carried out using the molecular dynamics software LAMMPS package.[54] The OPLS-AA force field is adopted to describe the potential environment in the TIPS-P crystal.[55] The details about the re-parameterized OPLS-AA force field will be illustrated later. Two types of ferroelasticity are examined by applying different loading conditions at 27°C. The model used in MD simulation for the ferroelasticity is built by expanding the lattice structure obtained from DFT calculation. The triclinic supercell has the size of 19.2 nm × 49.2 nm × 1.6 nm (along the X, Y and Z directions) and three tilt factor of xy = -7.33 nm , xz = 0.06 nm , yz = -0.48 nm , containing 140800 atoms. The lattice structure is energetically minimized and then fully relaxed under the NPT ensemble at 27°C and zero pressure for 0.5 ns. For FE1, a constant shear engineering strain rate of 0.02% per picosecond along the *x* direction is applied to the supercell model by changing the tilt factor of *xy* under NVT ensemble. For FE2, the *y*-direction tensile load is employed under NPT ensemble with a tensile engineering strain rate of 0.02% per picosecond, while the *x* length is allowed to shrink to preserve the product of *x* and *y* length as constant. The shear stress and shear strain along the $[\bar{1}20]$ direction in FE2 are calculated by performing the resolved plane stress/strain analysis illustrated in **Fig. S31**.[56] The recovery process is conducted by applying the reverse shear/tensile strain with an engineering strain rate of -0.02% until the resultant strain is reduced to zero. The periodic boundary conditions are applied to all three directions. The temperature and pressure are controlled using the Nosé–Hoover thermostat and barostat with a time step of 0.1 fs.[57]

Force Field Parameterization:

In the OPLS-AA force filed set, the total energy of the molecular system is calculated as the sum of multiple energetic terms for the harmonic bond stretching, harmonic angle bending, a Fourier series of torsional (dihedral and improper)energetics, and Coulomb and 12-6 Lennard-Jones potential for the nonbonded interactions, which are exhibited in the equation 1-4 accordingly.[55]

$$E_r = K_r (r - r_{eq})^2 \tag{1}$$

$$E_\theta = K_\theta (\theta - \theta_{eq})^2 \tag{2}$$

$$E_\phi = \frac{1}{2}V_1[1+\cos(\phi)] + \frac{1}{2}V_2[1-\cos(2\phi)] + \frac{1}{2}V_3[1+\cos(3\phi)] + \frac{1}{2}V_4[1-\cos(4\phi)] \tag{3}$$

$$E_{nb} = 4\varepsilon\left[\left(\frac{\sigma}{r}\right)^{12} - \left(\frac{\sigma}{r}\right)^{6}\right] + \frac{q_i q_j e^2}{r} \tag{4}$$

The required parameters are the bonding force constants K_r, the bending force constant K_θ, the equilibrium values for the bond length and bending angle r_{eq} and θ_{eq} , the Fourier coefficients V, the partial atomic charges, q, the Lennard-Jones radii σ where inter-particle potential is zero ,and the depth of the potential well ε. The symbols and atom types used in OPLS-AA force field are listed in the **Table S6** and also demonstrated in the molecular structure (**Fig. S32**). The atomic charges are calculated using the electrostatic potential (ESP) fitting method and assigned to each atom type shown in **Table S6** as well. The Lennard-Jones parameters for each atom type and most of the energetic parameters for the bond length, angles, dihedrals and impropers are adopted from the original OPLS-AA database.[55] However, several force field parameters associated with the *sp* carbon and silicon in TIPS-P molecule are missing. Specifically, they are, bond stretching parameters for the CZ^{I}-Si bond, the angle bending parameters for the CZ^{I}-Si-CT^{II} bond angle and CZ^{II}-CZ^{I}-Si bond angle, torsion energetic parameters for the CZ^{I}-Si-CT^{II}-CT^{I} dihedral and CZ^{I}-Si-CT^{II}-HC^{II} dihedral. The parameterization process is described as follows. We first examine the equilibrium values for the above bond length, bond angles and dihedral angles by applying the quantum mechanics calculations. The geometric optimization of TIPS-P molecule, the single-point energy calculations and also the partial charges calculations are all conducted using the GAUSSIAN09 program under the density functional theory level with the B3LYP hybrid functional and the 6-311++G(d,p) basis set.[46] The equilibrium bond length r_{eq}, angles θ_{eq} obtained from the optimized configuration are listed in the **Table S7** and **Table S8**. Next, to get the bonding/bending force constants and torsion Fourier coefficients, the energy scan of the specific bond, angle and dihedral are conducted by performing single-point energy calculations on varying bond length, bending angle and dihedral angle around their equilibrium values, respectively. The resulting changes in their conformational energy are fitted into the corresponding OPLS-AA bond stretching, bending angle and torsion energetics formula

(**Equation 1-3**). The good comparison between the ab-initio data and the fitted curves are demonstrated in the **Fig. S33**. The fitted parameters including the bonding/bending force constants and torsion Fourier coefficients are also shown in the **Table S7** and **S8**. The complete force field parameter set and the associated topological data of TIPS-P crystal are incorporated into the LAMMPS software by home-built codes.[54] A cutoff distance of 6Å is chosen for both the Lenard-Jones potential and long columbic interactions, which most stabilizes the lattice structure in the NPT ensemble (27°C and zero pressure) and gives the closest agreements with the experimental lattice data, based on current force field parameter set. **Fig. S33** demonstrates the temperature and pressure profile of Form I for the equilibrium 5 ps after running the NPT simulation at 27°C and zero pressure for 200 ps. The thermal fluctuations at the equilibrium states are well controlled with a standard temperature deviation of 1K and the average pressure is also well stabilized within a range of -2~2 MPa. Thus, we can believe that the new force field parameters would be suitable for the molecular dynamics simulation at ambient conditions.

Structural Descriptor and Order Parameter:

To investigate the molecular evolution of deformation twinning in ferroelasticity, it's vital to have the appropriate structural descriptor to identify different polymorphs. The determination of structural descriptor for TIPS-P molecular crystal is illustrated as below. Firstly, the "point molecule" scheme is used to extract the basic geometric information of one isolated TIPS-P molecule.[58] As shown in **Fig. S16a**, the center of mass position of the molecule is regarded as the origin and is labeled as r. The vector from the origin to the Si atom in the side group defines the z'-axis and the vector from the origin to the center of an adjacent aromatic ring is the y'-axis. The cross-product of the two vectors gives the direction of the x'-axis, which is perpendicular to the pentacene backbone plane. Next, we need to find the appropriate parameter to characterize the coordination environment of one molecule. From **Fig. S31**, we have learned that the major differences in the lattice structures of three polymorphs are the lattice length along *b*-axis and the lattice angle of γ. Those two lattice parameters are mainly associated with the molecular arrangements in the *ab* plane. Thus the structural descriptor is defined based on the molecular neighbor symmetry in one *ab* plane layer as depicted in **Fig. S16b**. Each molecule has four nearest-neighbor molecules with the center of mass r_i. The four center-of-mass distances can be defined as

$$d_i = \left| r_i - r_0 \right|, i = 1, 2, 3, 4 \tag{5}$$

According to the molecular symmetry, the center-of-mass distances are related as: $d_1 = d_3$, $d_2 = d_4$. At equilibrium states, the (d_2- d_1) (or d_4- d_3) for Form I, Form II and Form III are 2.5, 1.0 and 0.0, respectively. Considering the center-of-mass position always fluctuates due to the thermal effects, the quantity of $\rho = (d_2+ d_4)-(d_1+ d_3)$ is used as the structural descriptor for one TIPS-P molecule. During MD simulation of twinning deformation, the $(d_2+ d_4)-(d_1+ d_3)$ is reducing from the average value of 5 to 0, corresponding to the phase transition from Form I to Form III. After that, the structural descriptor ρ turns to be negative up to the average value of -5 which is identified as twinned Form I. In the twinned Form I, the $[\bar{1}10]$ axis (along d_2 direction) and [010] axis (along d_1 direction) swap so that the structural descriptor ρ is reduced to the value of -5. The switching of these two lattice vectors is also confirmed by the experimental measurements.

To characterize the smooth transition of twinning deformation in MD simulation, the order parameter is proposed as below with the structural descriptor as inputs.

$$\xi_\rho = \begin{cases} 0 & \rho_i \geq \rho_h \\ \frac{1}{4}(1-\cos(w_i)) & \rho_l < \rho_i < \rho_h \\ 0.5 & -\rho_l \leq \rho_i \leq \rho_l \\ 1-\frac{1}{4}(1-\cos(w_i)) & -\rho_h < \rho_i < -\rho_l \\ 1 & \rho_i \leq -\rho_h \end{cases} \quad \text{, with } w_i = \frac{\pi(|\rho_i| - \rho_h)}{\rho_l - \rho_h} \qquad (6)$$

In the above equation, ξ_ρ is the order parameter for a given structural descriptor ρ_i. The $cos\,(\omega_i)$ function is chosen so that its derivative is zero at $\pm\rho_l$ and $\pm\rho_h$ shows a smooth transition between those values. The value of ρ_h is selected as 4.5 which is slightly smaller than the equilibrium value of 5.0 of Form I while the value of ρ_l is determined as 2.0 to indicate the formation of intermediate phase (Form III). Those values are chosen to reduce the effects of normal thermal vibrations of molecules around their equilibrium states. **Fig. S34** illustrates the variation of the structural descriptor ρ of each molecule in three polymorphs resulting from the thermal vibrations at 27°C. Specifically, for Form I, the number of ρ vibrates around 5.0 with a small deviation value of 0.5. Thus the molecules with the structural descriptor higher than 4.5 will be regarded as the Form I. Form II has the mean value of 2.0 with a standard deviation of 1.0 while the average ρ value of Form III is around 0.0 with a large deviation of 2.The thermal vibrations of the structural descriptors indicates that the thermodynamic stability of Form I is much better than that of Form II and Form III at 27°C. Besides, the range of the structural descriptors of Form II and Form III overlap so that the transition from Form II to Form III can easily happen. Thus the intermediate phase appearing in the twinning transition is simply identified as Form III phase which may override the possibility of mixed Form II and Form III phases. The color coding of MD simulation scenarios is done by calculating the order parameter (**Equation 6**) for each molecule, ranging from 0 (green) to 1 (blue). The green represents the original Form I, red stands for the intermediate Form III and blue represents the twinned Form I.

Cooperative motions:

Rotational and displacive motions of backbone

The cooperative rotational and displacive molecular motions of ferroelastic transition are elucidated in **Fig. 3d** and **4d**, respectively. Based on the "point molecule scheme" (**Fig. S16**), the rotational angle of one molecule φ_t at time *t* is calculated as below,

$$\varphi_t = \cos^{-1}(\vec{y}_o \cdot \vec{y}_t')$$

Here, $\overrightarrow{y_o}$ is the unit vectors of molecular *y* axis (backbone direction) at original state. $\overrightarrow{y_t'}$ is the unit vector of molecular *y* axis at time *t* projected onto the plane determined by $\overrightarrow{y_o}$ and $\overrightarrow{r_o r_t}$ (vector connecting the center of mass of molecules at two states). **Fig. 3d** shows the temporal evolution of rotational angles for four neighbor molecules in one (010) layer, in accordance with the lattice transition from Form I (green) to intermediate (red) and eventually twinned Form I (blue) in FE1. The **Fig. 4d** demonstrates the concurrent displacive motions of four molecules in one (210) layer in FE2. The displacement is calculated as the travelling distance of the center of mass of one molecule at time *t*.

Supporting Text 1. Polarized Raman Microscopy

We evaluate the orientations of the pentacene core before and after transition by measuring polarized angle dependent intensity of the peak at 1571 cm^{-1}, which is normalized by peak intensity at 1369 cm^{-1} (**Fig. 3c**). These vibrational modes correspond to C-C ring stretching of pentacene along the long and short axis of the molecule, respectively (**Fig. S13**); thus, normalized intensity maximizes when incident polarized laser aligns with the molecular long axis. In the FE1 transition case, the result informs molecular reorientation by 40 – 50° rotation (the intensity maximum is found at the polarization angle of 215° for pristine and 170° for deformed domain; **Fig. 3c**). By the same method, we evaluate the in-plane orientation change of the pentacene core upon FE2 transformation. It is found that normalized intensity of 1571 cm^{-1} peak maximized at the almost the same polarization angle for both pristine and deformed domains (**Fig. 4c**). The results are in good agreement with the inference from SC-XRD for both FE1 and FE2 cases.

Supporting Text 2. Cross-Polarized Optical Microscopy

In addition to SC-XRD, the axis switching behavior is further verified using CPOM analysis. As shown in **Fig. 3b**, the deformed crystal by FE1 transition shows characteristic angles γ (81.6°) and ω (49.1°) in the pristine and twinned domains, respectively. These angles correspond well to crystallographic angles between (100) and (010) planes for γ and (110) and (010) facets for ω of Form I (**Fig. 3a**). The result indicates that the side facet changes from (100) to (110), as a result of the axis switching behavior. Similarly, axis switching upon FE2 transition is verified by CPOM analysis. As described in **Fig. S23** and **Fig. 4a**, between the side facet and (210) transformation boundary, angles ψ (28.6°) and φ (21.0°) are shown in pristine and deformed regions, characteristic of crystallographic angles between (100) and (210) facets for ψ and (110) and (210) facets for φ, respectively. The result also indicates that the side facet changes from (100) to (110) by the axis switching behavior.

Supporting Text 3. Molecular Dynamics Simulation (FE2)

We have carried out MD simulation by applying y-axis (i.e., [010]) tension at 27°C on Form I, which exclusively resulted in FE2 based lattice reorientation (**Movie S8**). **Figure 4d** shows representative structural configurations from the stress-strain loop in **Fig. 4e**. The resolved shear stress induced by the tensile loading triggers the molecules to glide along molecular long-axis direction, whose vector is parallel to the transformation interface, (210). The appearance and the role of the intermediate Form III interface layers are essentially identical to that in the FE1 case—i.e., it mediates two distinctively oriented lattices at the interface, and molecular trajectory passes through this phase before an accomplishment of full transformation. Similar to the FE1 case, axes switching is clearly observed in the simulation (magnified view in **Fig. 4d**). However, distinct from the FE1 twinning process, the emergence of twinning zone as well as the intermediate Form III transformation is mainly described by the cooperative molecular gliding. **Figure 4f** shows synchronized molecular displacement of four molecules in a molecular layer, signifying cooperative nature of the transformation.

Supporting Text 4. Cross-Polarized Optical Microscope Study on Flexible Electronic Devices.

CPOM study carried out in parallel offers direct evidence for tension induced twin domain formation and evolution in our single crystal devices. **Figure S28** presents the optical micrographs at the different strain states of Form I crystal device in **Fig. 5a**. The image from ε = 1.27% exhibits nucleation and propagation of twin domains indicated by white arrows, implying that the crystal already yields at a strain below 1.27%. Further extension of crystal increases the number of twin domains (ε = 2% – 5%), and at the same time increases the width of existing twin domains. In this regime, we observe a persistent but slight decrease in conductivity, which is most likely due to axes switching from $[010]$ to $[\bar{1}10]$. Meanwhile, microcrack-tip formation at the twin boundary is observed (see a white dotted circle in **Fig. S21**, **S28**). These partially-disconnected transport paths—almost uniformly distributed across multiple twinning sites—are circumvented at the early stage of deformation (ε = 0% – 5%) thanks to two-dimensional transport in TIPS-P crystals. However, further extension of crystals (ε = 7% – 13%) leads to noticeable crack progression at certain microcracks by concentrated stress field (red circle in **Fig. S28**), causing precipitous drop in conductivity. Despite the microcrack tip formation, reversibility of conductivity is still achieved (**Fig 5b**) due to reversible thickening and thinning (or elimination) of twinned domains without increasing the microcrack size during mechanical cycling (**Fig. S29**). In contrast to the Form I case, Form Ib crystals manifest no observable crack-tip formation and progression even at high strain (**Fig. 5c**), exhibiting remarkably high tolerance to mechanical strain of the device. The molecular mechanism of this phenomenon will be pursued in a future study.

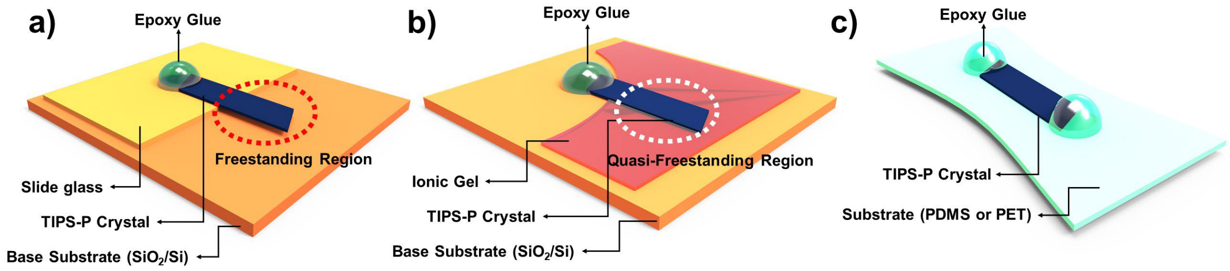

Scheme S1. Schematic illustrations of (thermo-)mechanical test specimens. a) Single-crystal with a jumping board configuration, b) single-crystal on an ionic gel substrate, and c) single-crystal on a deformable substrate (PDMS or PET). For all the configurations, crystals are fixed using epoxy glue at the crystal tip(s).

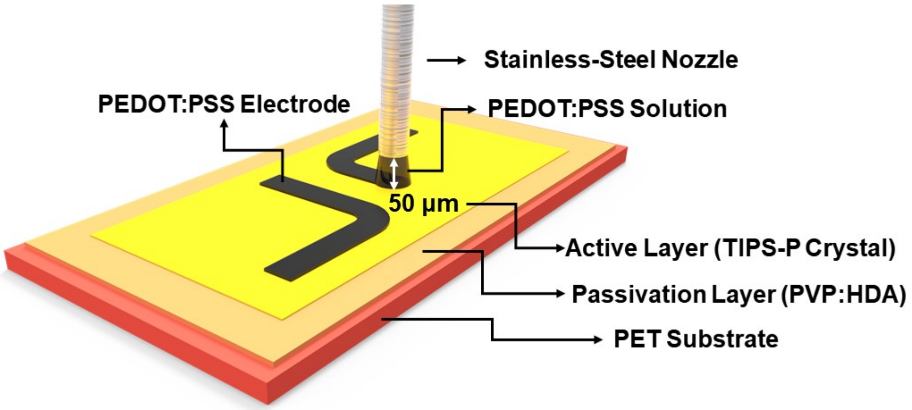

Scheme S2. Schematic illustrations for the conductive-ink deposition method. PEDOT:PSS electrode printing is performed on the basis of 3D printer setup.

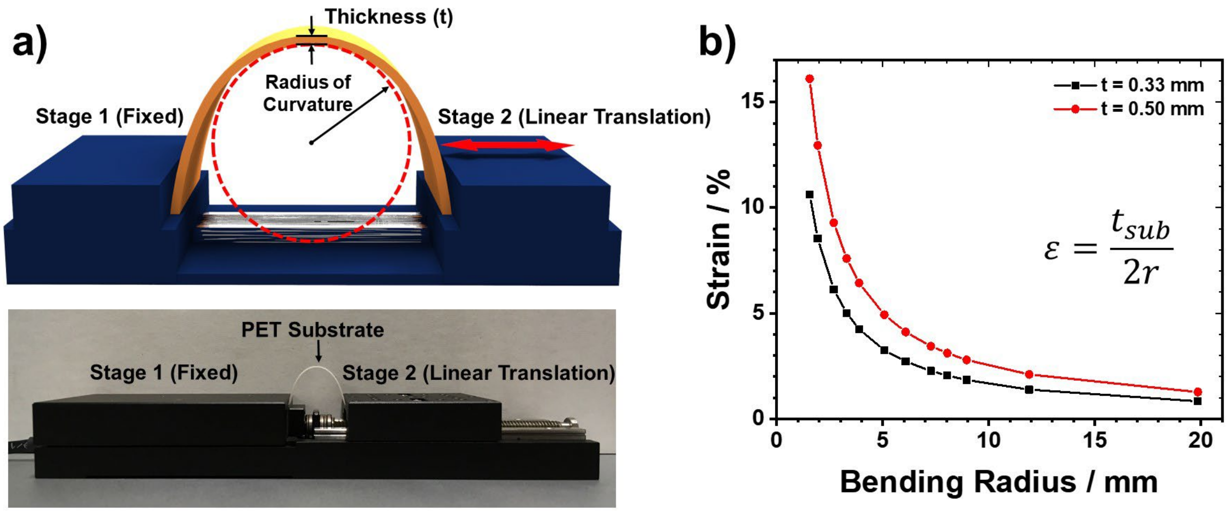

Scheme S3. **a** Schematic illustration and photograph for tensile bending stage/experiment. Thickness (t) of the PET substrate for bending experiments is either 0.33 mm or 0.50 mm. **b** Bending radius versus strain plots for PET substrates with different thicknesses (black: t = 0.33 mm; red: t = 0.50 mm).

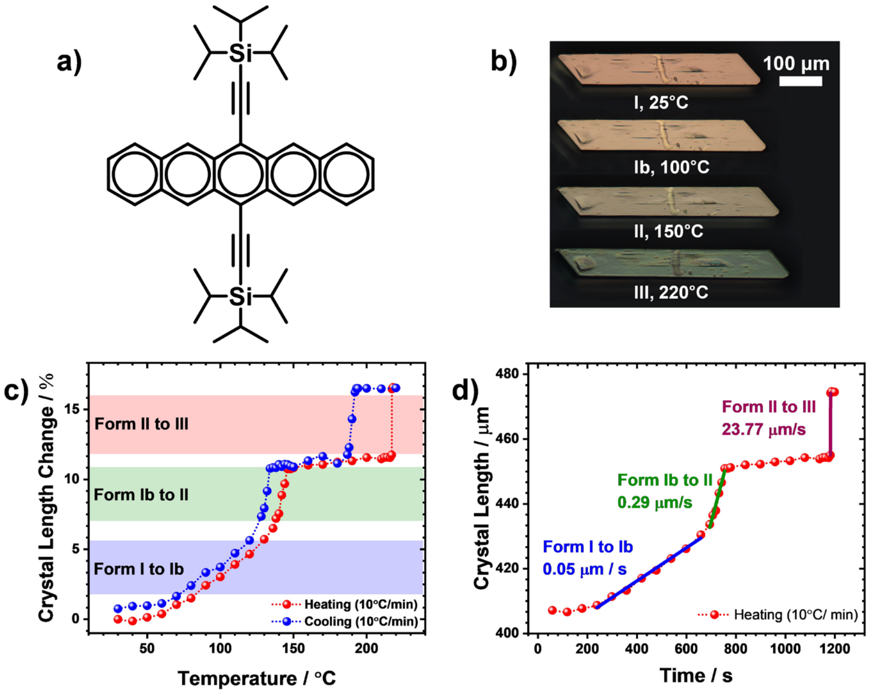

Fig. S1. Thermoelasticity of TIPS-P crystal. **a** Molecular structure of TIPS-P. **b** Representative CPOM images of TIPS-P crystal at different temperature conditions which leads to thermoelastic phase transitions and shape change of the crystal (long-axis elongation). **c** Plot to illustrate temperature dependent length change of the crystal. The heating and cooling rate is 10°C s^{-1}. First order transitions (Form I(b)–II and II–III) lead to a steep increase (decrease) in the length upon heating (cooling); whereas, second order transition (Form I – Ib) leads to a gradual change in the length of crystal. The transitions are fully reversible. **d** Time versus crystal length plot upon thermoelastic transitions. Gradual transformation is observed at the temperature range of ca. 65 – 120°C suggesting second-order transition (Form I–Ib), and two abrupt transformation were observed at ca. 130 – 140°C and 220°C by first-order transitions (Form I(b)–II and Form II–III, respectively).

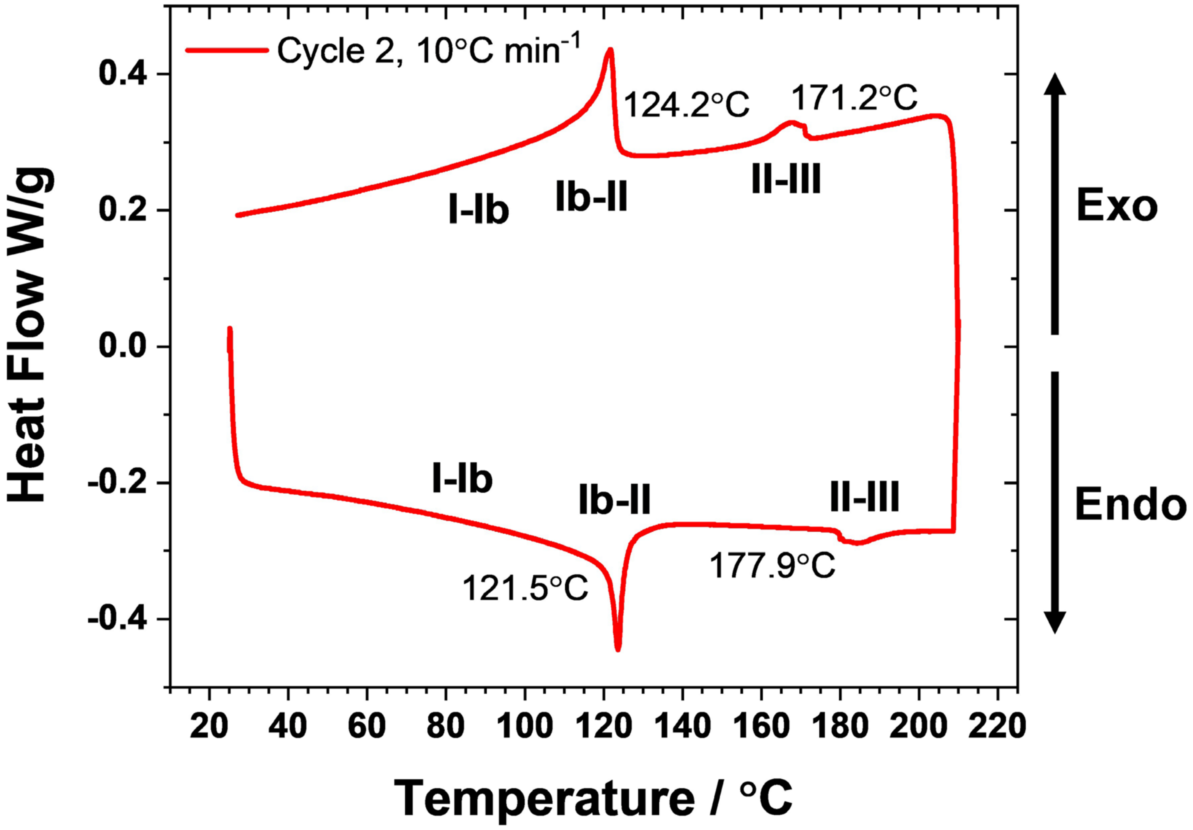

Fig. S2. The DSC result of TIPS-P (second cycle, with a heating/cooling rate of 10°C min^{-1}). Two first-order transitions start at 121.5° and 177.9° are shown, which we assign those transitions as I(b)-II and II-III, respectively. Apparent slope change is also observed around 60 – 115°C, indicating the second-order nature of I-I(b) transition. The temperature differences between DSC and CPOM study are originated from the temperature-control setup of the optical microscope.

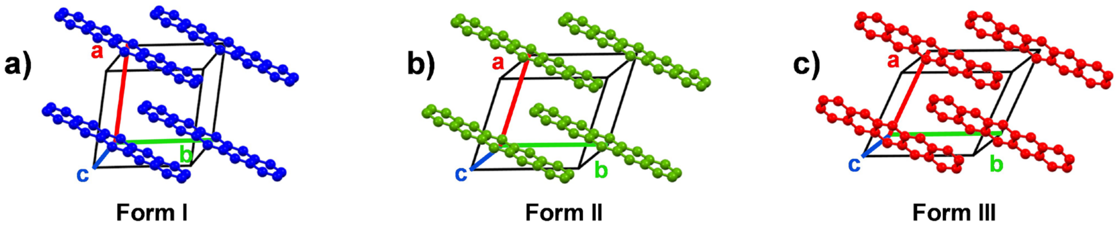

d)

	Form I[a]	Form II[b]	Form III[c]	Twinned Form I[d]
Chemical Formula	C44H54Si2	C44H54Si2	C44H12Si2[e]	C44H54Si2
Formula Weight	639.05	639.05	596.7508[e]	639.05
Temperature/ °C	27°C	127°C	169°C	25°C
Crystal system	Triclinic	Triclinic	Triclinic	Triclinic
Space group	P-1	P-1	P-1	P-1
Unit cell dimensions	7.76 Å	7.60 Å	7.60 Å	7.76
	7.74 Å	8.58 Å	8.99 Å	7.73
	16.95 Å	17.23 Å	17.27 Å	16.93
	77.87°	78.22°	82.24°	77.89
	88.54°	86.71°	89.91°	88.50
	82.20°	72.10°	65.16°	82.20
Volume / Å^3	986.71	1046.5	1058.2	982.8
Density	1.075	1.014	0.597[c]	1.080
Z	1	1	1	1
theta range for data collections	2.46 to 25.50°	2.42 to 18.00°	2.16 to 9.86°	2.31 to 14.44°
Reflections collected	15410	5599	8043	22033
Completeness to theta	99.90%	98.60%	93.40%	94.00%
Refinement method	Full-matrix least-squares on F2	Full-matrix least-squares on F2	Full-matrix least-squares on F2	Full-matrix least-squares on F2
Data / restraints / parameters	3665 / 92 / 245	1426 / 707 / 347	1190 / 69 / 23	3397 / 244 / 73
GOF	1.114	2.773	4.327	1.059
Final R indices	R1: 0.0526, wR2: 0.1414	R1: 0.1226, wR2:0.3396	R1 0.3196, wR2: 0.7228	R1: 0.0458, wR2:0.1239
R indices (all data)	R1: 0.0661, wR2: 0.1526	R1: 0.1494, wR2:0.3560	R1: 0.3407, wR2: 0.7480	R1: 0.0549, wR2: 0.1364

[a] The Form I structure is drawn by switching the *a*- and *b*-axes from the reported structure (ccdc: 1570910), so that the π-stacking axes of all structures are fixed to the *b*-axis. This is to minimize confusion caused by axes switching during phase transition. [b] ccdc: 1570911, [c] *Supplementary Structure 1*, ccdc 1991343. [d] *Supplementary Structure 2*, ccdc 1991344. [e] Because of very limited observed electron density in the rotator side chain part, we simulate the structure without including hydrogen atoms in this unit. It is particularly due to the dynamic nature of the side chain, whose atomic constituents are not spatially confined in the structure.

Fig. S3. Single crystal X-ray structures of TIPS-P polymorphs. **a** Form I, **b** Form II, and **c** Form III. Considering lattice symmetry of the structures, they are restructured to show structural registry between phases. **d** The table summarizes crystallographic data and refinement statics for these structures as well as twinned Form I obtained through FE2 transformation. It is well understood that martensitic transition features the diffusionless and displacive nature of the transformation with close structural similarity and registry. Crystal structures reported (Form I and II) and resolved (Form III) through variable temperature in-situ SC-XRD indeed reveal such attributes. All the polymorphic phases of TIPS-P show P-1 symmetry based on the 2D-brickwork packing motif, however with the considerable displacement of molecules along π-plane (see noticeable changes in the lattice parameters *b* and *γ*).

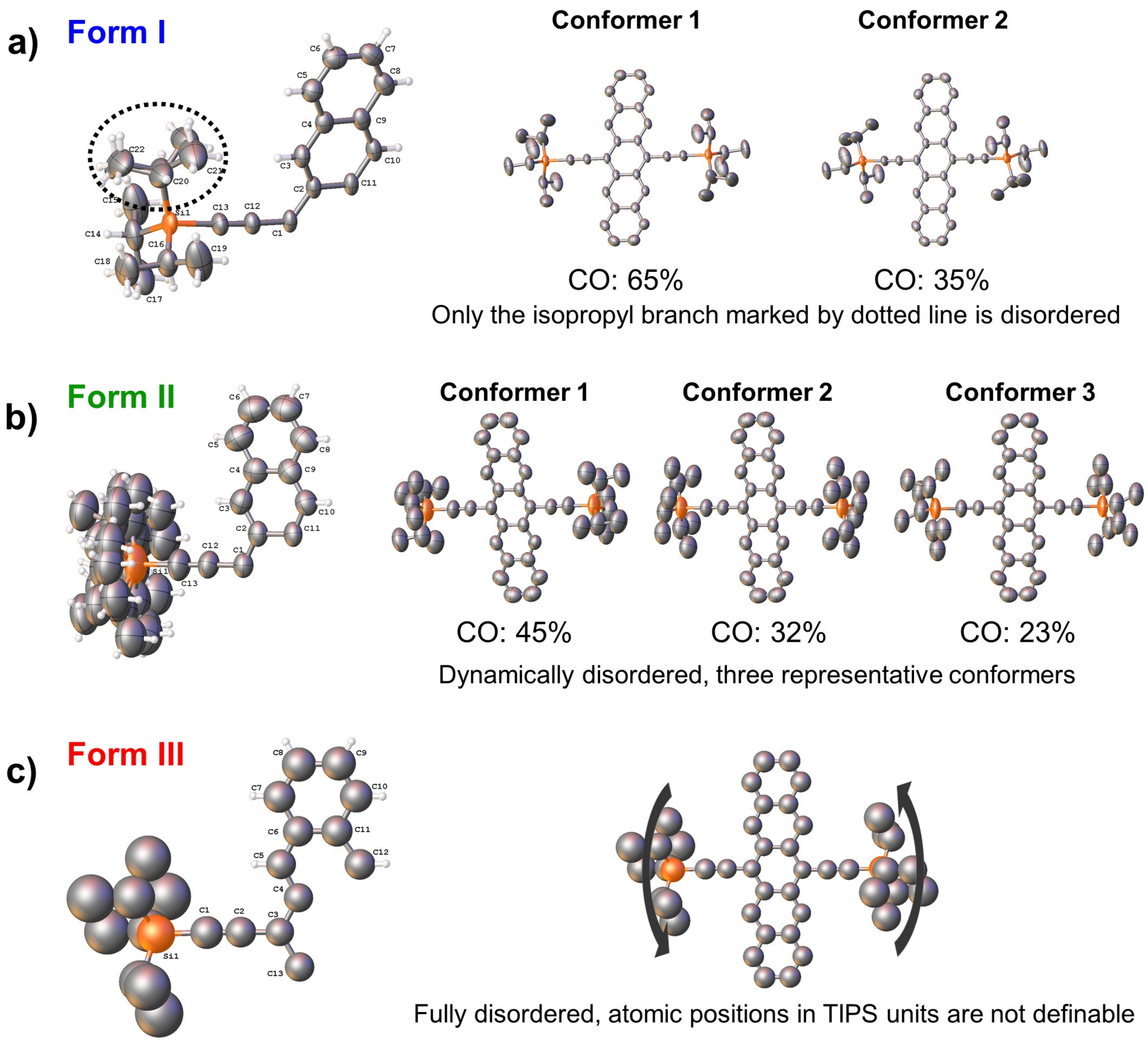

Fig. S4. The ORTEP plots (50% probability) for TIPS-P structures. Hydrogen atoms in the conformational isomers are omitted to clarify the structures. **a** The position of the atoms that constitute TIPS units is well defined in the Form I structure. Only one of the isopropyl branches is disordered in Form I (black dotted circle). Two conformational isomers are found, showing chemical occupancy (CO) of 65% and 35%, respectively. **b** Side chain of Form II are disordered exhibiting three distinct conformational states with chemical occupancy of 45%, 32% and 23%, respectively. **c** TIPS units Form III are fully disordered. It is strongly evidenced by observed electron density map (**Fig. S5**), exhibiting negligible electron density for isopropyl units (thus, the hydrogen atoms of TIPS units cannot be resolved). The simulated conformational state in **c** should be understood as one of various probable states.

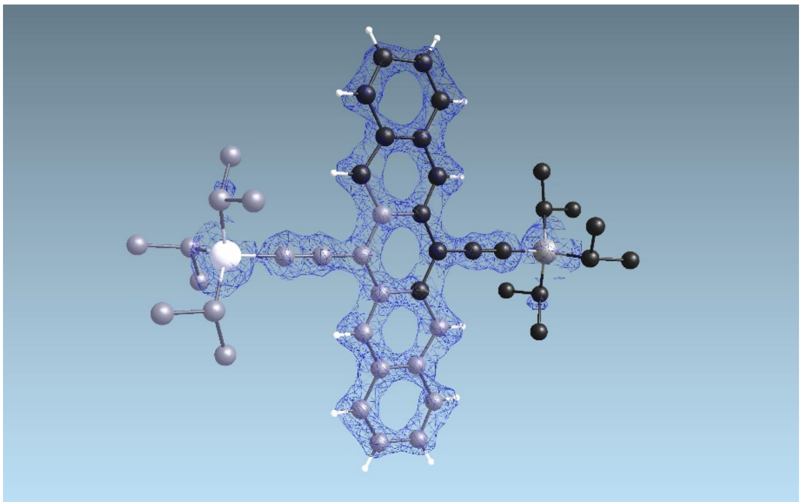

Fig. S5. Observed electron density map for the full TIPS model in the Form III structure. It manifests diffused or negligible electron density in the side chain units, indicating disordered nature of TIPS unit. The F_{obs} contours are drawn at the 0.86 electrons per cubic angstrom level.

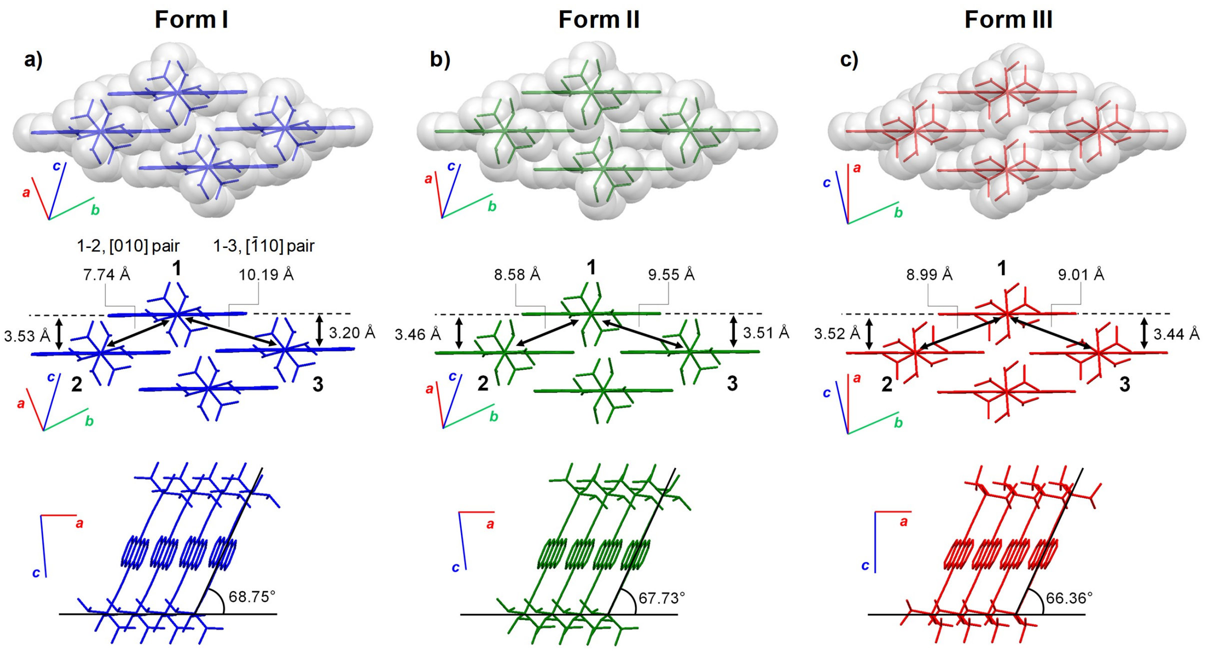

Fig. S6. Comparison of molecular packing in the unit cells of TIPS-P **a** Form I, **b** Form II and **c** Form III polymorphs. Top panel: the space-fill representation of each polymorphic structure. Middle panel: comparison of centroid-to-centroid distances and interplanar π- π distances measured in $[010]$ and $[\bar{1}10]$ pairs across polymorphs. Bottom panel: comparison of molecular tilting angles across polymorphs.

Among the four different polymorphs of TIPS-P (i.e., Form I, Ib, II and III), the structures of Form I, II and III are fully resolved; where molecular packing and associated intermolecular interactions in Form I structure has been widely studied in the field of molecular/crystal engineering.[59] By introducing bulky TIPS side-chains onto the pentacene, the molecular packing shifts from herringbone to layered two-dimensional arrangement, where the molecules excellently fill the physical space formed upon the introduction of the bulky side-chain substituents (top panel). Such molecular packing is stabilized by weak intermolecular interactions between neighboring pentacene cores as well as side-chains, due to the layered structure that separates well the pentacene and TIPS layers (bottom panel). Between neighboring pentacene cores, so called π-π interaction appears, where the interplay between stabilizing dispersion energy and destabilizing exchange energy terms will determine the stable molecular arrangement in terms of short-, long-axis molecular slip and interplanar π-π distance.[45] Similarly, interactions between neighboring side-chains occur, which are also based on attractive dispersion and repulsive exchange terms.[45] In the high-temperature polymorphs (Form II and III), however, entropy contribution becomes increasingly important,[41] as represented by considerable disorder in the rotator side-chains (**Fig. S4**,**S5**). Therefore, rearrangement of molecular packing occurs at high temperatures, which can be mainly described by changes in centroid-to-centroid distances measured in $[010]$ and $[\bar{1}10]$ pairs (middle panel). Particularly, centroid-to-centroid distance between $[010]$ increases from 7.74 Å to 8.58 Å by I-II transition and 8.58 Å to 8.99 Å by II-III transition. The separation of this pair is indicative of providing more space around TIPS units for their rotational motion. In addition to that, slight changes in the interplanar π-π distance (middle panel) and tilting angle (bottom panel) are observed upon polymorphic transitions, while two-dimensional brickwork arrangement is overall well maintained.

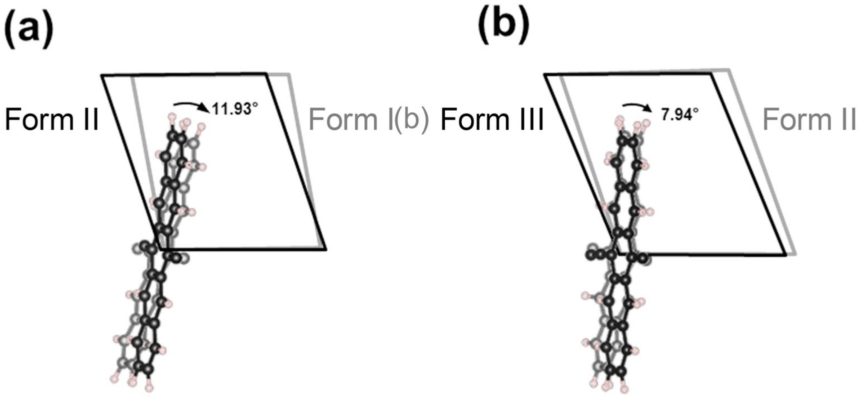

Fig. S7. AIMD predicted molecular rotation upon superelastic transitions. **a** Clockwise rotation by 11.93° and **b** by 7.94° are observed by SE1 and SE2, respectively.

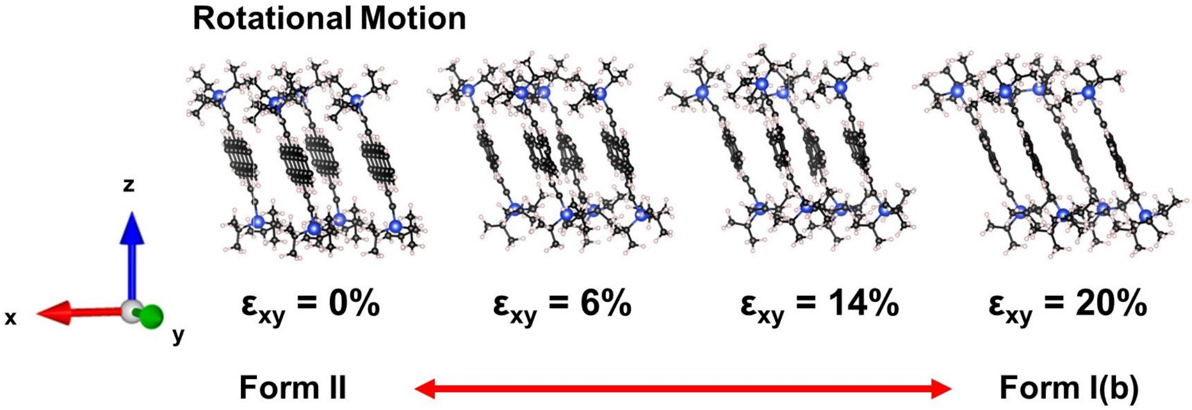

Fig. S8. AIMD simulated molecular motion investigated upon SE1 transition at 127°C (y-axis view). Rotational motion is clearly observed in this y-axis view.

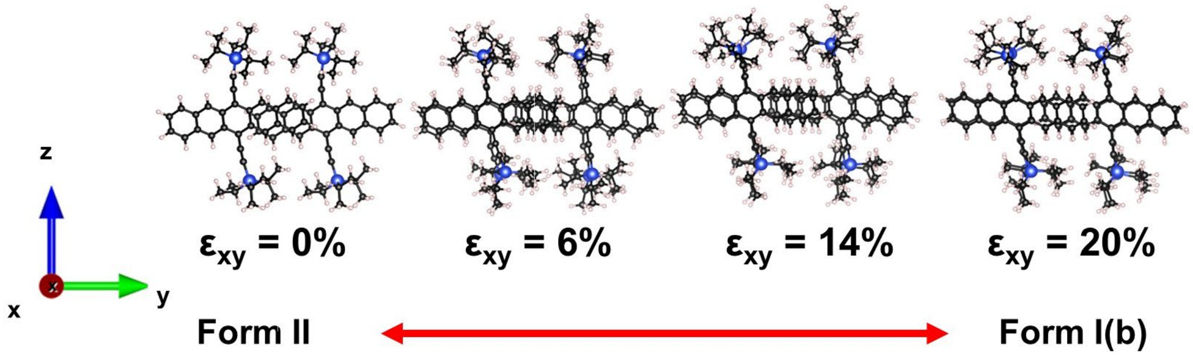

Fig. S9. AIMD simulated molecular motion investigated upon SE1 transition at 127°C (x-axis view).

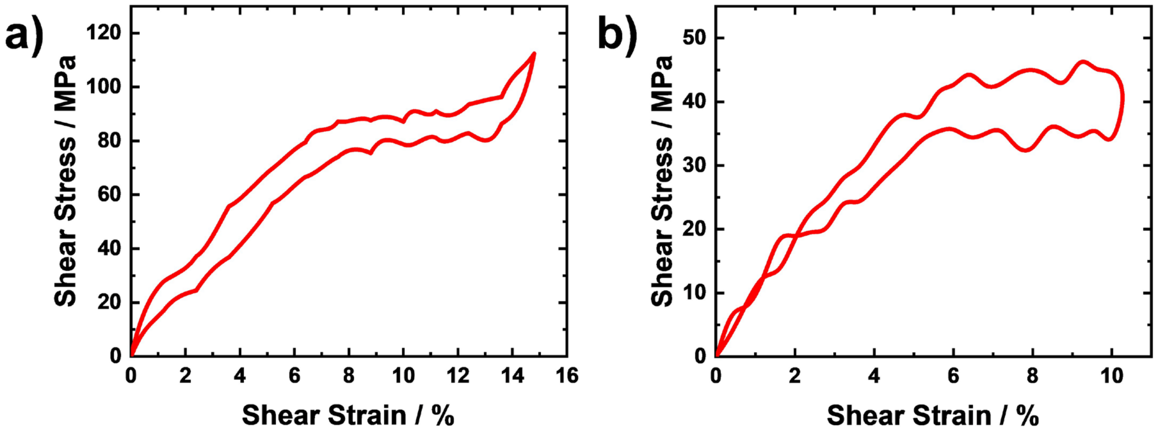

Fig. S10. The DFT calculated strain-stress curves for **a** SE1 and **b** SE2 transitions by the static shear loading.

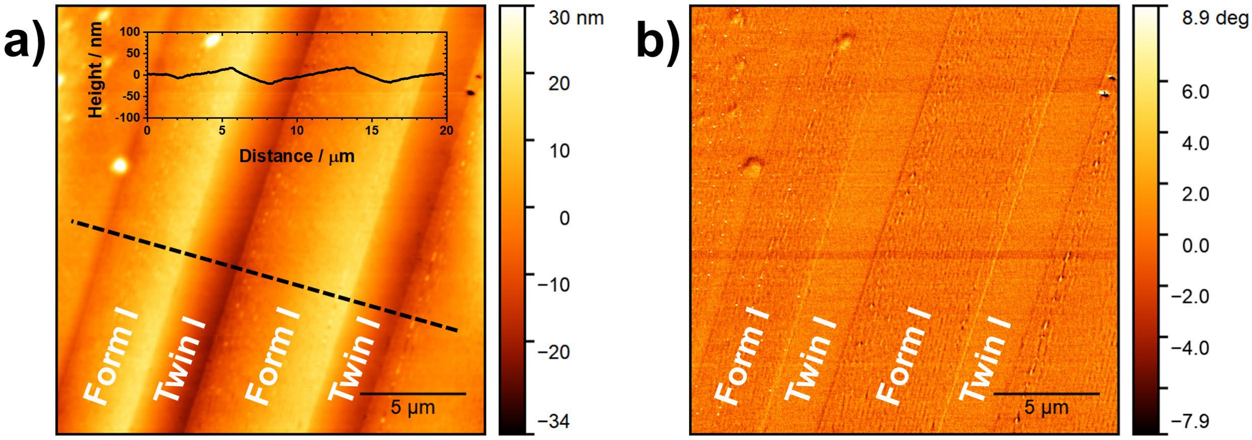

Fig. S11. Atomic force microscope images taken from deformed TIPS-P crystal through FE1 transition. **a** a height mode image exhibiting slight slope changes at transformation boundary, see inserted height versus distance profile (along black dashed line). **b** a phase mode image that shows slight changes in the contrast at the twinned regions.

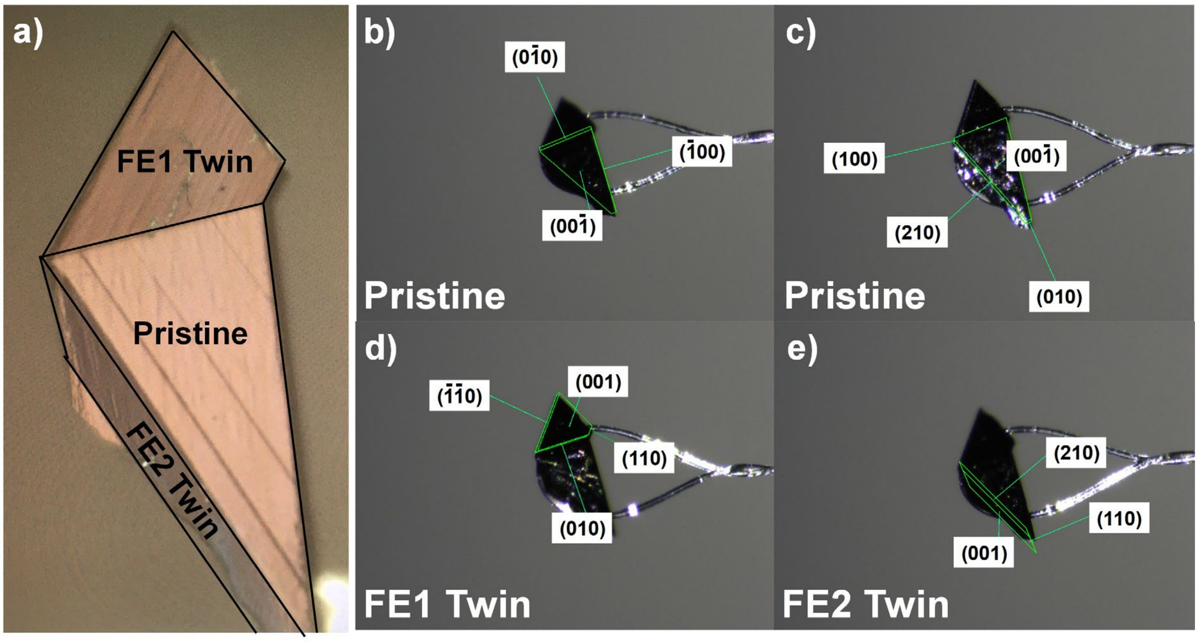

	a	b	c	α	β	γ
Pristine	7.694	7.675	16.965	75.65	88.06	82.15
FE1	180°-Rotation about a (010) plane normal, i.e., [-0.13, 1, -0.094], with the twinning interface of (0-10)$_P$/(010)$_T$					
FE2	180°-Rotation about [-120] with the twinning interface of (210).					

Fig. S12. Orientational relationships and indexed facets of Form I crystal after FE1 and FE2 transitions. **a** CPOM image of the crystal used in this study. Crystallographically determined habit planes of the pristine domain (**b**, **c**), FE1 twin (**d**), and FE2 twin (**e**). The facets are indexed using Bruker APEX 3 software. The table beneath shows cell constants of the pristine domain, and the orientational relationship between the pristine and the twinned domain for both FE1 and FE2. Using *Cell Now*, it is found that FE1 twin is reoriented by 180°-rotation about (010) plane normal, i.e., [-0.13 1.0 -0.094], with an interfacial habit plane of (010). In the case of FE2 twin, lattice reorientation is accomplished through 180°-rotation about [-120] with an interfacial habit plane of (210).

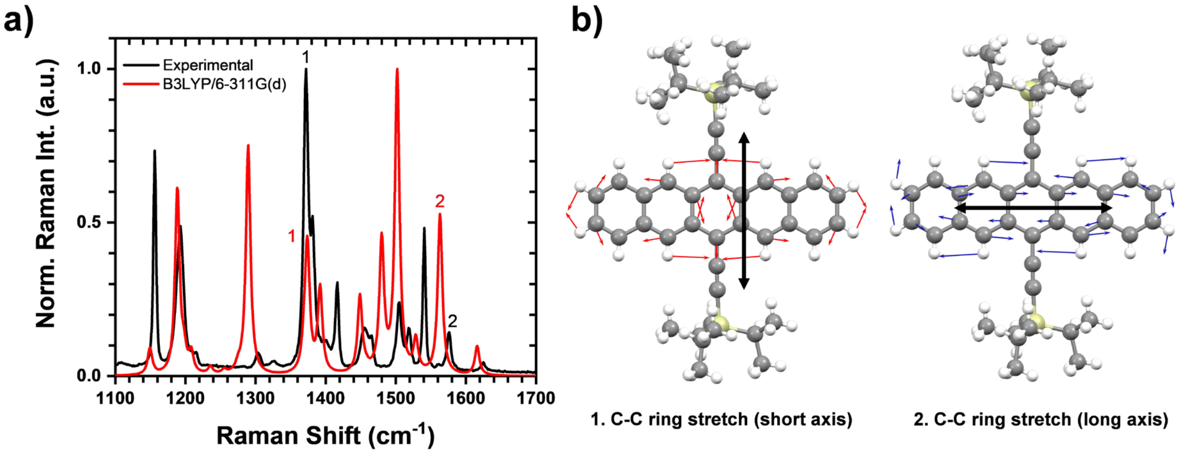

Fig. S13. **a** Experimental and theoretical Raman spectra of TIPS-P, (black line: the experimental spectrum of TIPS-P crystal using 785 nm laser excitation; red line: DFT calculated Raman spectrum of gas phase TIPS-P molecule at the B3LYP/6-311G(D) level of theory). The Raman frequency of computational spectrum is calibrated based on a scaling factor of 0.966. **b** Simulated atomic displacements for the Raman peaks (1: 1369 cm^{-1} and 2: 1571 cm^{-1}), whose peak positions are indicated in the experimental/theoretical spectra in **a**. Black arrows in **b** denote the direction of polarization for these selected vibrational modes.

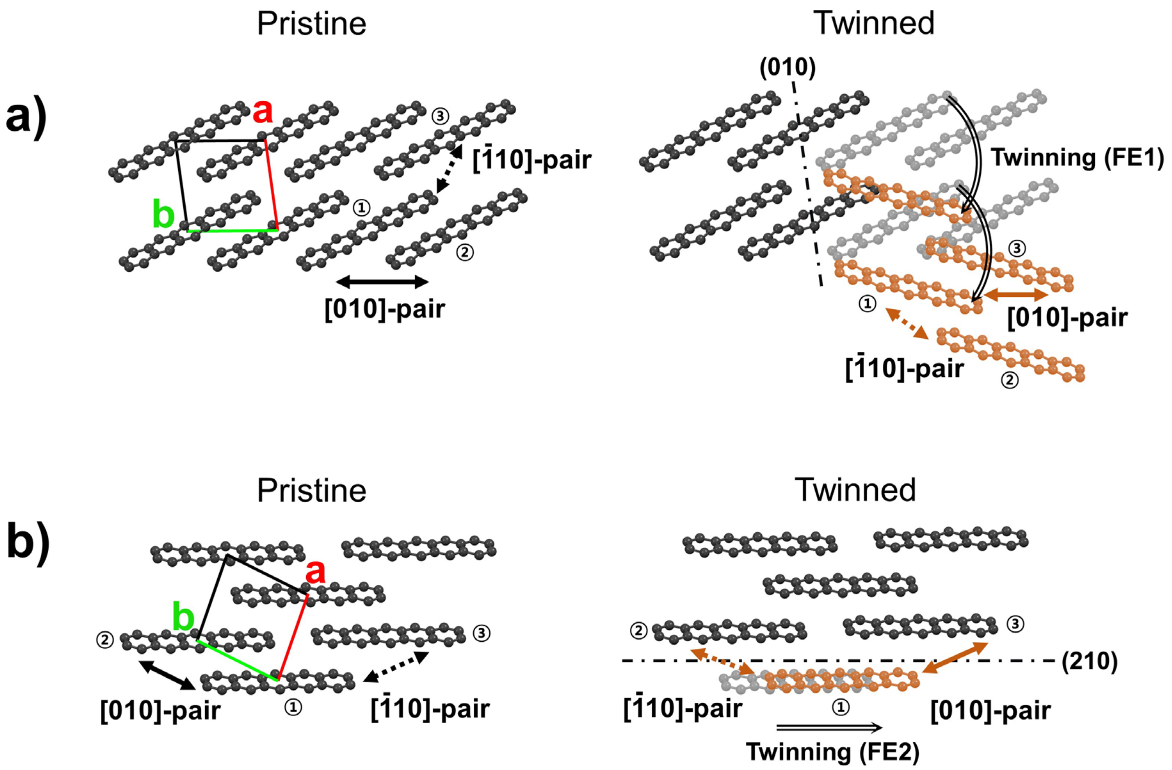

Fig. S14. Schematic illustrations of the π-stacking axes switching mechanism based on **a** FE1 and **b** FE2 transition (black molecules: molecules in the pristine structure, orange molecules: molecules in the twinned state). As depicted in the pristine structures (left), molecules 1 and 2 constitute $[010]$-pair (dimer along the main π-stacking axis); whereas molecules 1 and 3 establish $[\bar{1}10]$-pair (dimer along the secondary π-stacking axis). On the one hand, after ferroelastic transitions (right), dimers based on molecules 1 and 2 become $[\bar{1}10]$-pair; whereas dimers based on molecules 1 and 3 become $[010]$-pair. Such π-stacking axes switching behaviors are confirmed by morphology analyses as well as molecular dynamic simulations.

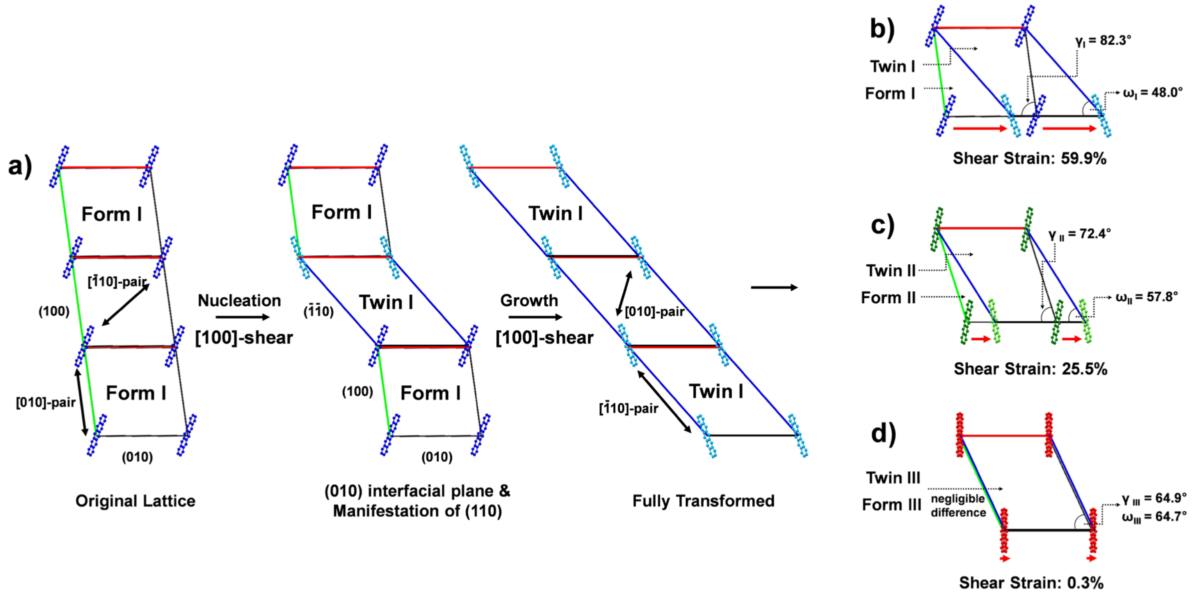

Fig. S15. Lattice representations of FE1 induced twinning processes. **a** Layer-by-layer FE1 transition behavior on the basis of Form I structure is schematically summarized. Experimental observations of (010) as the twin boundary and manifestation of (110) plane as the side facet in twinned regions are reflected in this schematic illustration. **b-d**. Overlaid lattices (*c*-axis view) before and after FE1 transition in Form I, II and III, respectively. Characteristic crystallographic angles (γ and ω) and predicted recoverable shear strains are denoted for each phase. The shear strain values in **b-d** are calculated as the changes in the angles (in radians), i.e., $\gamma - \omega$ in the corresponding structures.

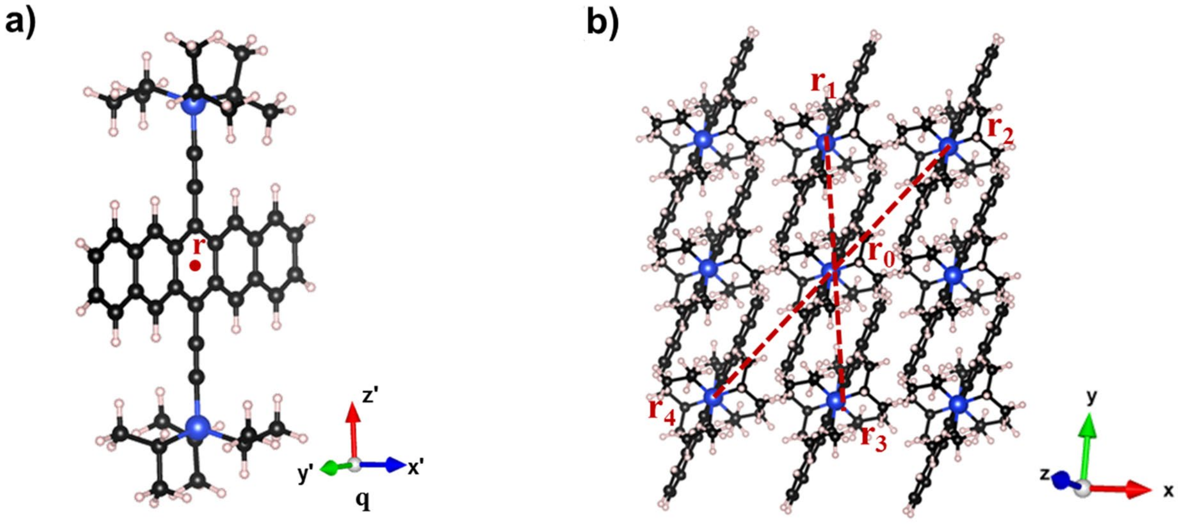

Fig. S16. a The point molecule scheme of TIPS-P. **b** The center-of-mass distances between the center molecule and its four nearest neighbor molecules used to define the structural descriptor.

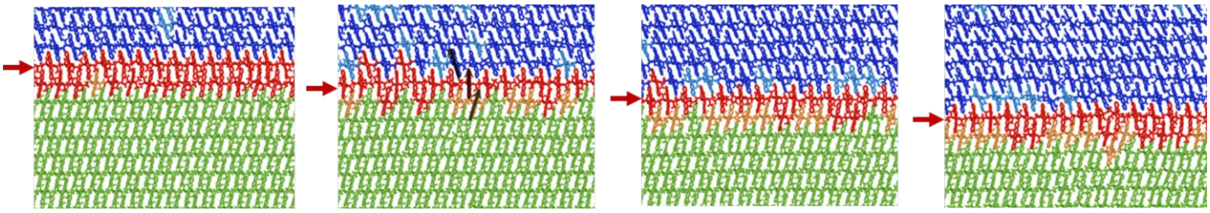

Fig. S17. Layer-by-layer twin growth in FE1. The red arrows indicate the transformation boundary, while the black arrows show the rotational angle differences for the pristine (green), intermediate Form III (red) and twinned Form I molecules (blue).

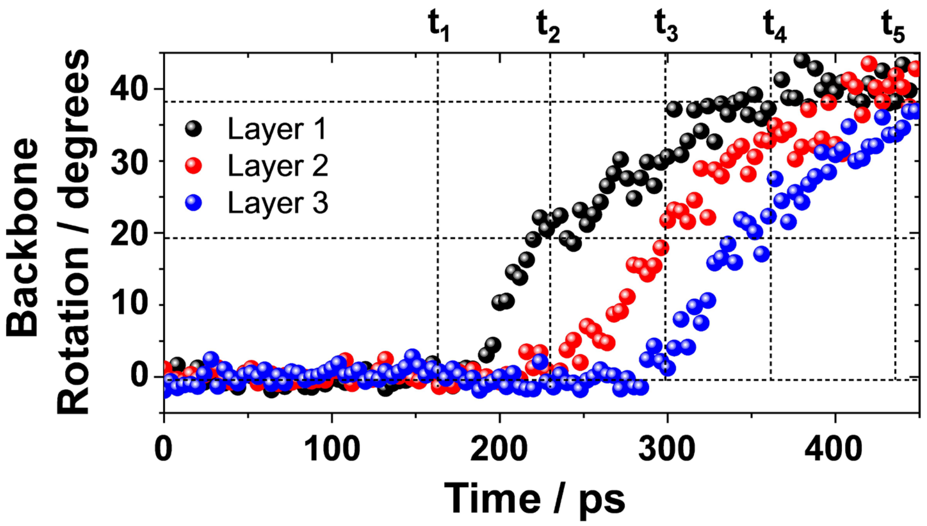

	t_1	t_2	t_3	t_4	t_5
Layer 1	**0 deg**	**19 deg**	**38 deg**	**38 deg**	**38 deg**
Layer 2	**0 deg**	**0 deg**	**19 deg**	**38 deg**	**38 deg**
Layer 3	**0 deg**	**0 deg**	**0 deg**	**19 deg**	**38 deg**

Fig. S18. Time dependent rotational angle evolution of three adjacent (010) molecular layers, upon forward FE1 transformation. Characteristic times t_1 – t_5 are indicated by vertical dotted lines; and characteristic angles (i.e., 0°, 19°, and 38° indicating Form I, III, and twinned I, respectively) are indicated by horizontal dotted lines. The plot clarifies layer-by-layer correlated transformation (or molecular rotation) by showing well-established transformation sequence, as summarized in the table below. For instance, between t_2 – t_3, Layer 1 rotate from 19° to 38° while adjacent Layer 2 rotate from 0° to 19°.

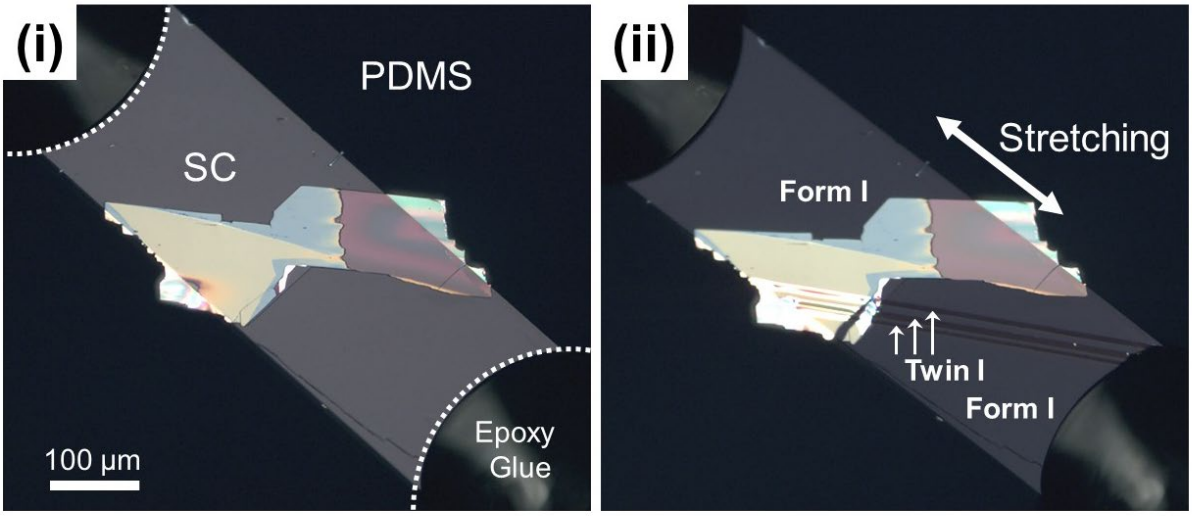

Fig. S19. Polarized optical micrographic images before (i) and after (ii) FE2 transformation, induced by uniaxial stretching.

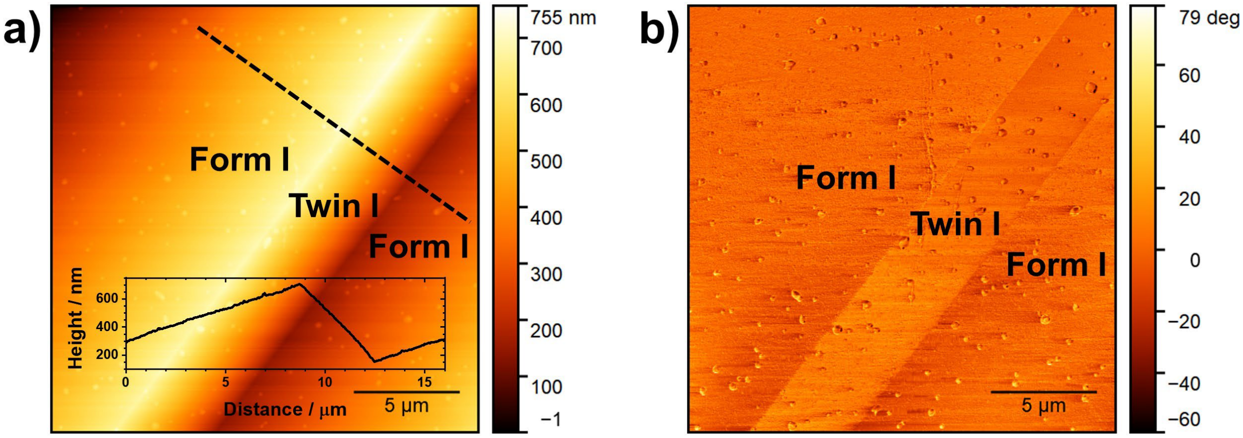

Fig. S20. Atomic force microscope images obtained from deformed TIPS-P crystal through FE2 transition. **a** Height mode image taken at the transformation boundary. The inserted height versus distance profile in **a** (along black dashed line) shows a slight slope change as it passes through transformation boundaries. **b** Phase mode image in the corresponding region of **a**.

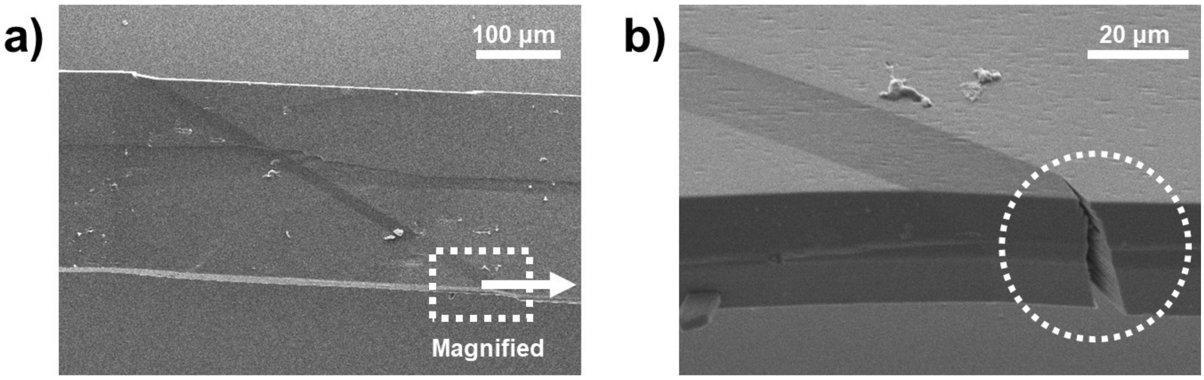

Fig. S21. Scanning electron microscope images taken from deformed TIPS-P crystal based on FE2 transition. Microscale crack-tip formation is observed as shown in b (marked by white dotted circle).

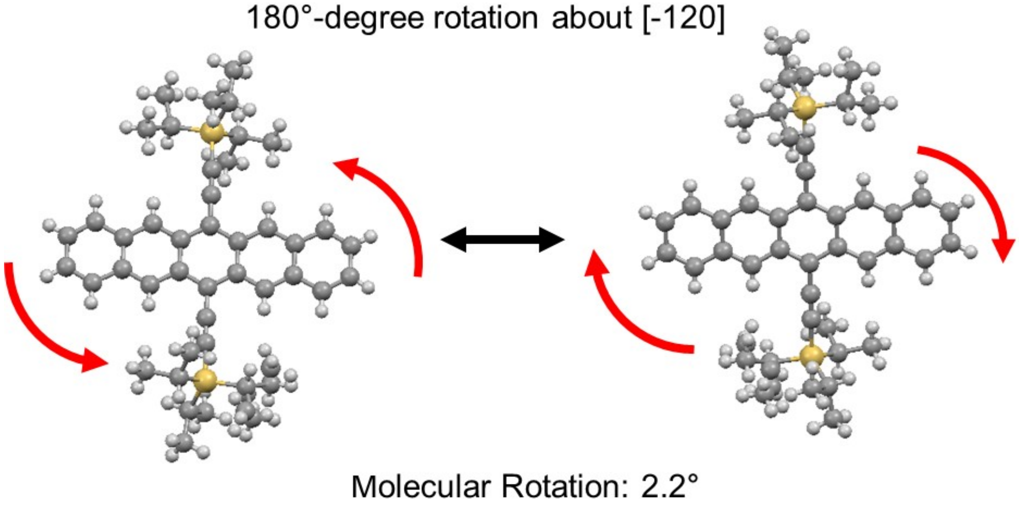

Fig. S22. Molecular rotation with respect to a π-plane normal upon FE2 transition by 180°-rotation about [-120] vector. Theoretical rotational angle is predicted to be 2.22°.

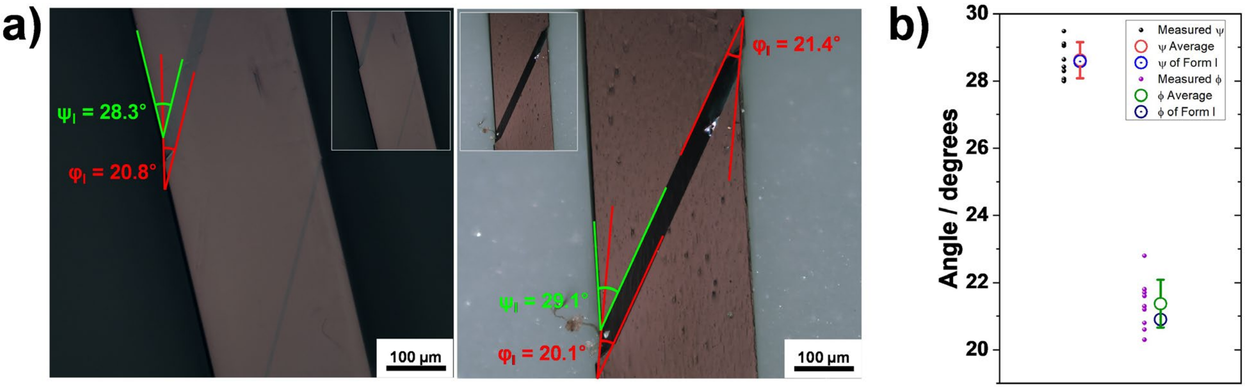

Fig. S23. Characteristic angles (ψ and φ) at the transformation interface of deformed crystals (FE2). **a** Polarized microscope images of twinned crystals obtained through tensile bending. **b** Angles are measured from ten different samples, giving average ψ of 28.6° (red circle) and φ-angle of 21.4° (green circle). Theoretical ψ (28.6°, blue circle) and φ of Form I (21.0°, navy circle) matches well with the average values.

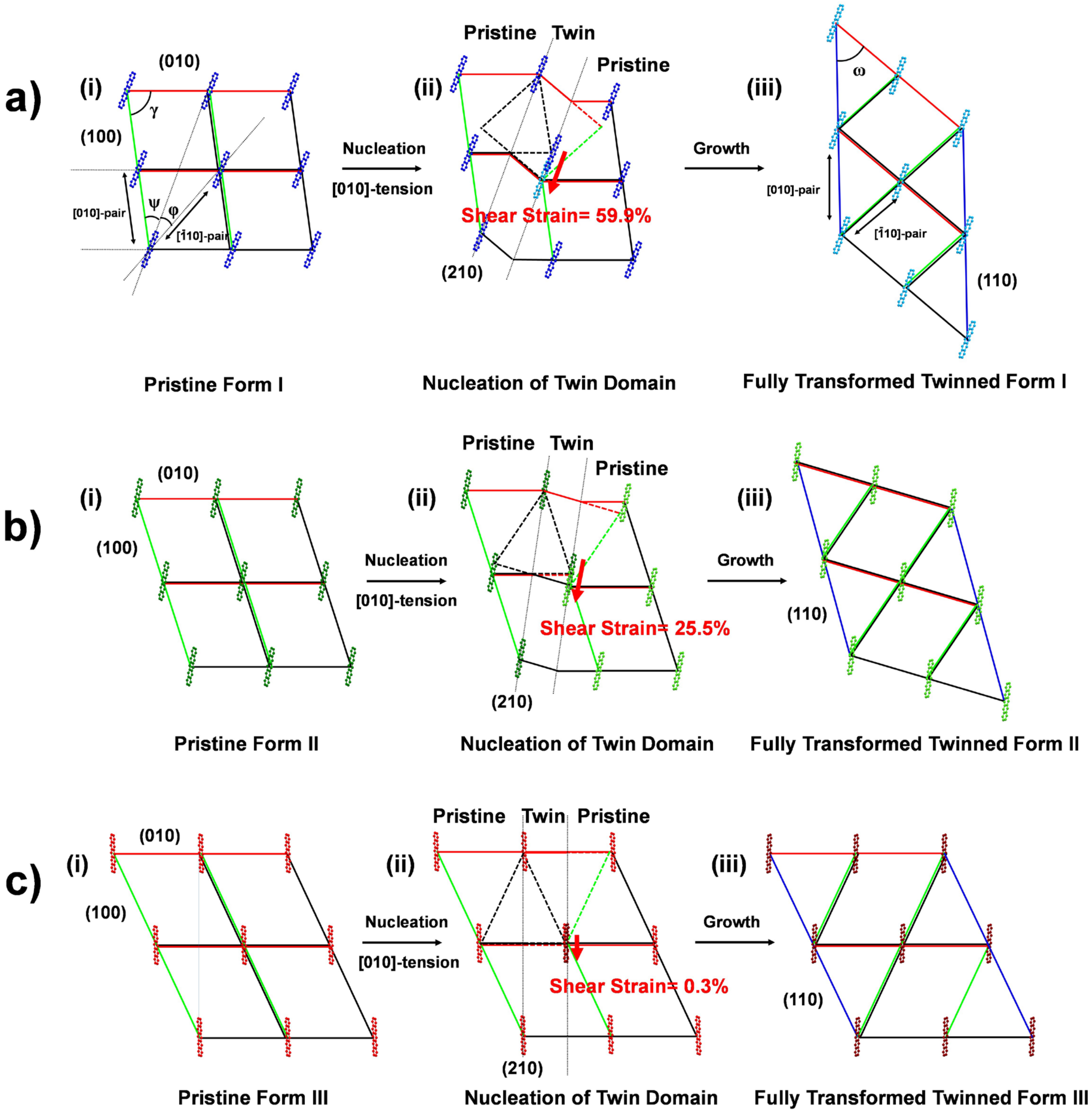

Fig. S24. Stepwise schematic illustrations for twinned domain evolution via the FE2 mechanism based on **a** Form I, **b** Form II and **c** Form III structures. (i) Original lattice structure of each form before transition. (ii) Nucleation of twinned domain based on molecular displacement along the (210) plane. (210) transition interface and recoverable strain is denoted in each phase. (iii) Fully transformed twinned state. (110) plane is manifested as side facets at this stage. The shear strain values in **a**-**c** are calculated as the changes in the angles (in radians), i.e., $\gamma - \omega$ in the corresponding structures.

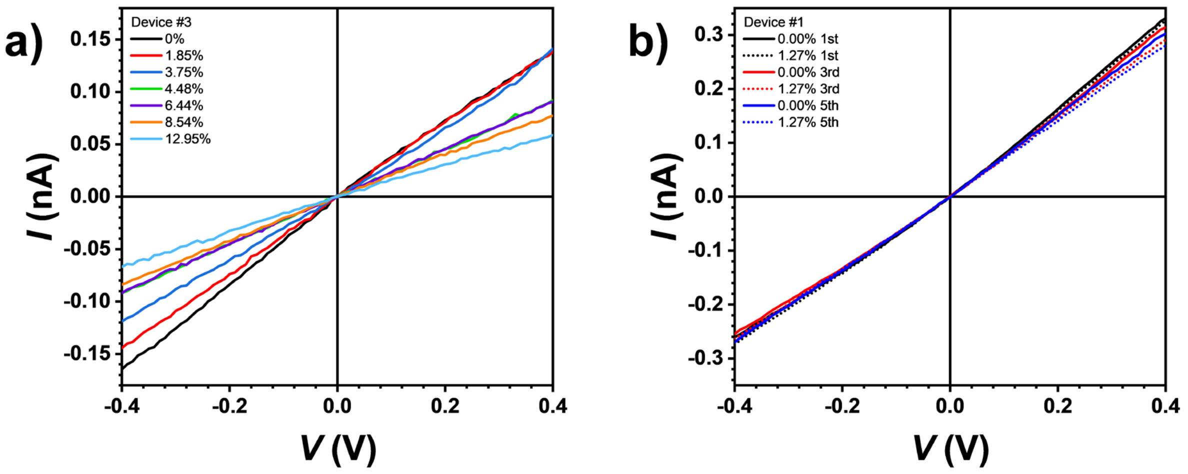

Fig. S25. Representative I-V curves upon Type-1 and Type-2 electrical measurement (Form I). **a** Tensile strain dependent I-V characteristic (Device #3 in **Fig. S26a**). **b** Cycling tensile strain dependent I-V characteristics (Device #1 in **Fig. 6b**).

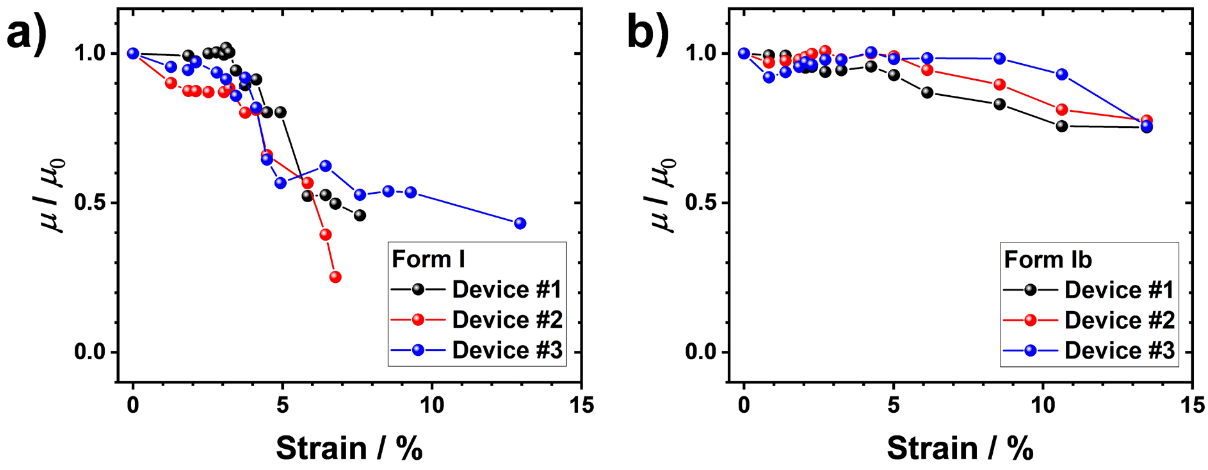

Fig. S26. Tensile strain dependent μ / μ_0 plot (Type-1) based on **a** Form I and **b** Form Ib crystals.

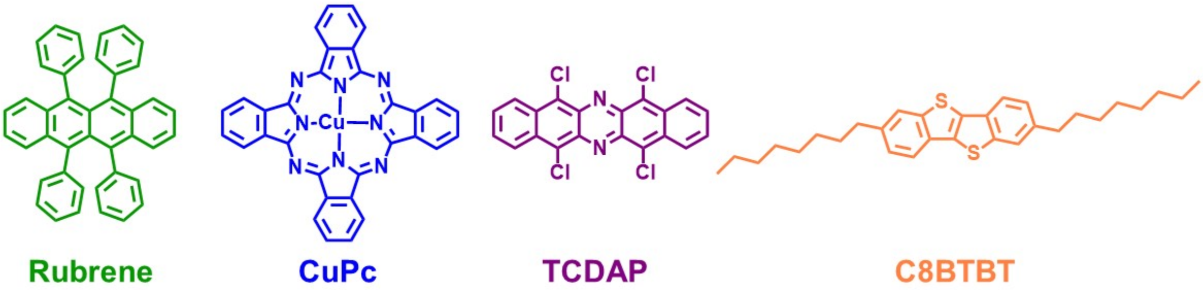

Fig. S27. Molecular structures of reference molecular semiconductor materials.

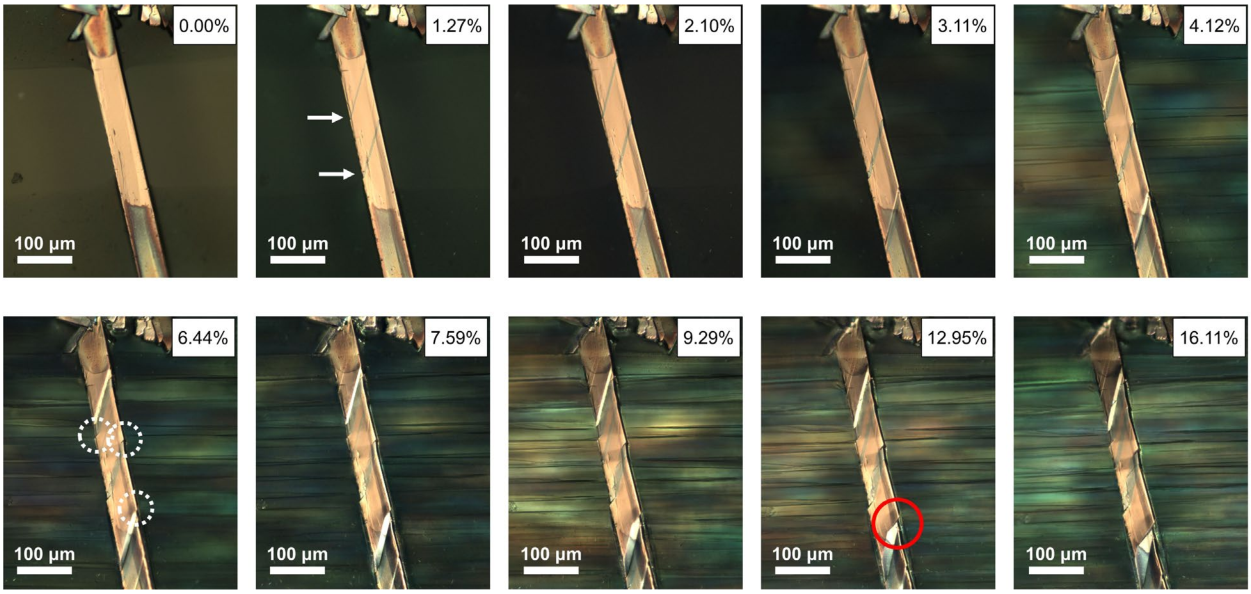

Fig. S28. Representative polarized optical microscope images taken in parallel while performing Type-1 measurement test (device #3 in **Fig. S25a**). Strain of about 1.27% leads to thin twinned domains formation (greenish striations indicated by white arrow). Micrographs based on strain ranges of 1.27% - 16.11% exhibited both twin domain growth and additional nucleation. In the image with strain of 6.44%, propagated crack-tips are found as indicated by the white dotted circles, some of which largely progressed at a higher strain condition (red circle in 12.95%).

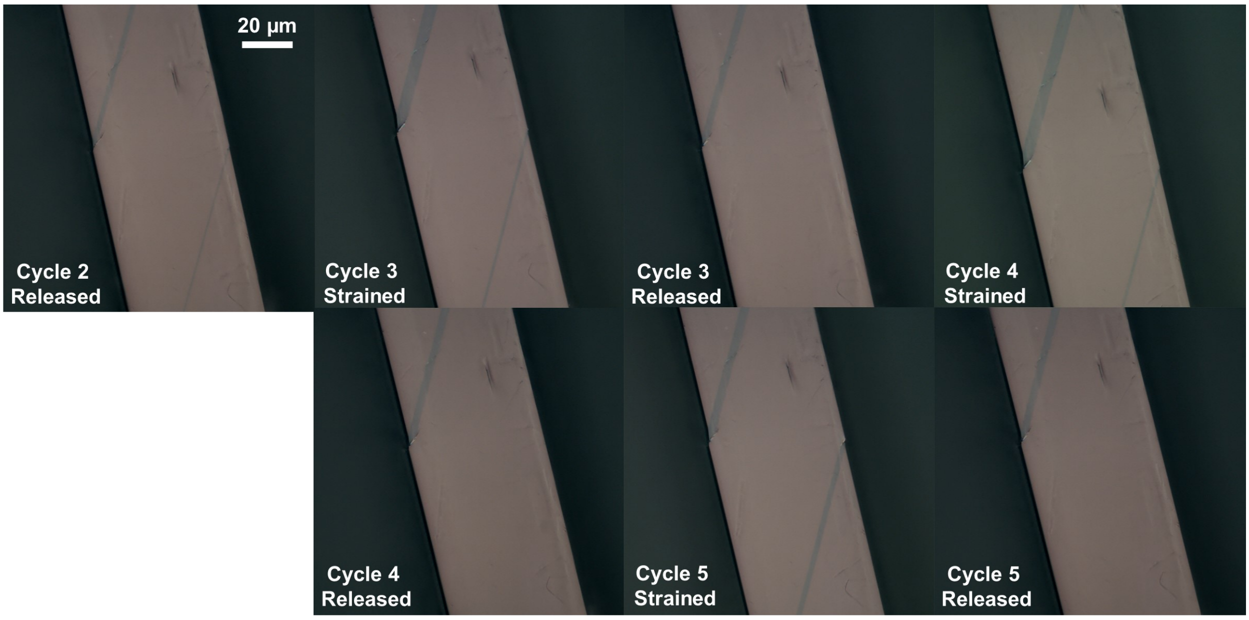

Fig. S29. Representative polarized optical micrographs taken in parallel while performing Type-2 measurement test (Cycle2 – Cycle 5 for device #1 in **Fig. 6b**). Growth of twin domains is shown in the strained states, whereas, released states result in a domain thinning (top domain) or a full removal of the twinned domain (bottom domain).

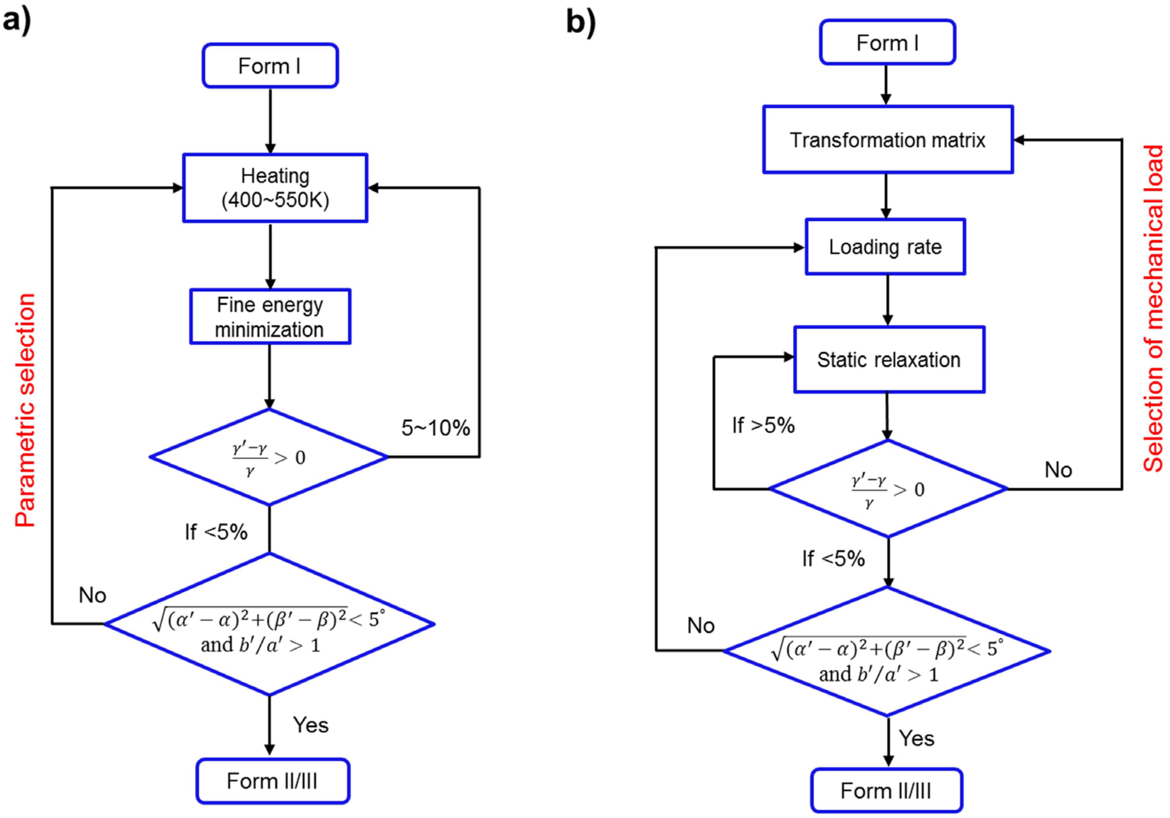

Fig. S30. Structural searching algorithms for the unit-cell polymorphic transition during **a** heating and **b** mechanical loading in DFT simulation.

$$\tau_{(2\,1\,0)} = -\frac{1}{2}(\sigma_x - \sigma_y)\sin 2\theta + \tau_{xy}\cos 2\theta$$

$$\varepsilon_{xy}^{(2\,1\,0)} = \sin\theta\cos\theta(\varepsilon_{yy} - \varepsilon_{xx}) - \cos 2\theta\varepsilon_{xy}$$

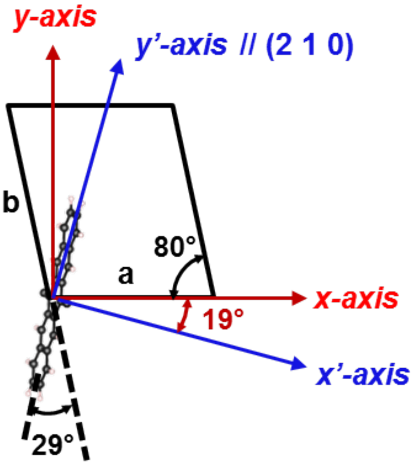

Fig. S31. The resolved shear stress and shear strain at (210) plane in FE2 are calculated based on the above equations (left). Here the value of $\theta = 19°$ is deduced from the analysis of geometric relations (right),where $\theta = 90° - (180° - 80° - 29°)$. The lattice angle γ is 80° for Form I and the angle between the b axis and (210) plane (along backbone direction) is 29°. The stress and strain components σ_x, , σ_y, , τ_{xy}, , ε_{xx} , ε_{yy}, , ε_{xy}, are all obtained from MD simulation of FE2.

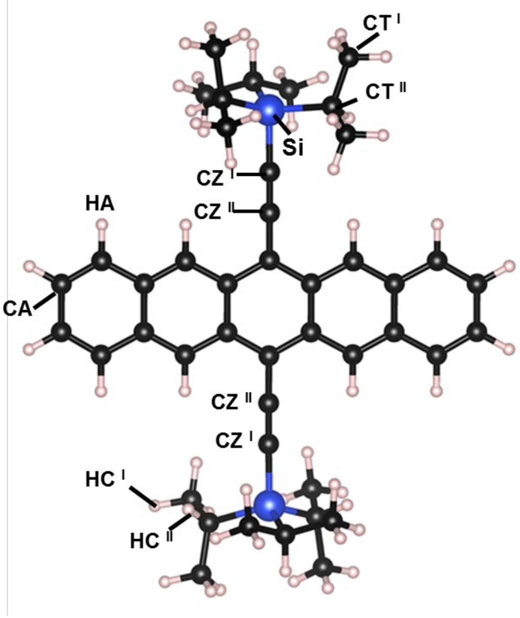

Fig. S32. The atom symbol of OPLS-AA force field assigned to each atom in TIPS-P molecule. **CA** and **HA** are for carbon atom and hydrogen atom of pentacene backbone, respectively. **CT$^{\mathrm{I}}$** and **HC$^{\mathrm{I}}$** are for carbon atom and hydrogen atom of the methyl group in the TIPS unit, respectively. **CT$^{\mathrm{II}}$** is for carbon atom connecting Si atom and two methyl groups in the TIPS unit. **HC$^{\mathrm{II}}$** is for hydrogen atom bounded to **CT$^{\mathrm{II}}$** atom. **CZ$^{\mathrm{I}}$** and **CZ$^{\mathrm{II}}$** are for the *sp* carbon atoms.

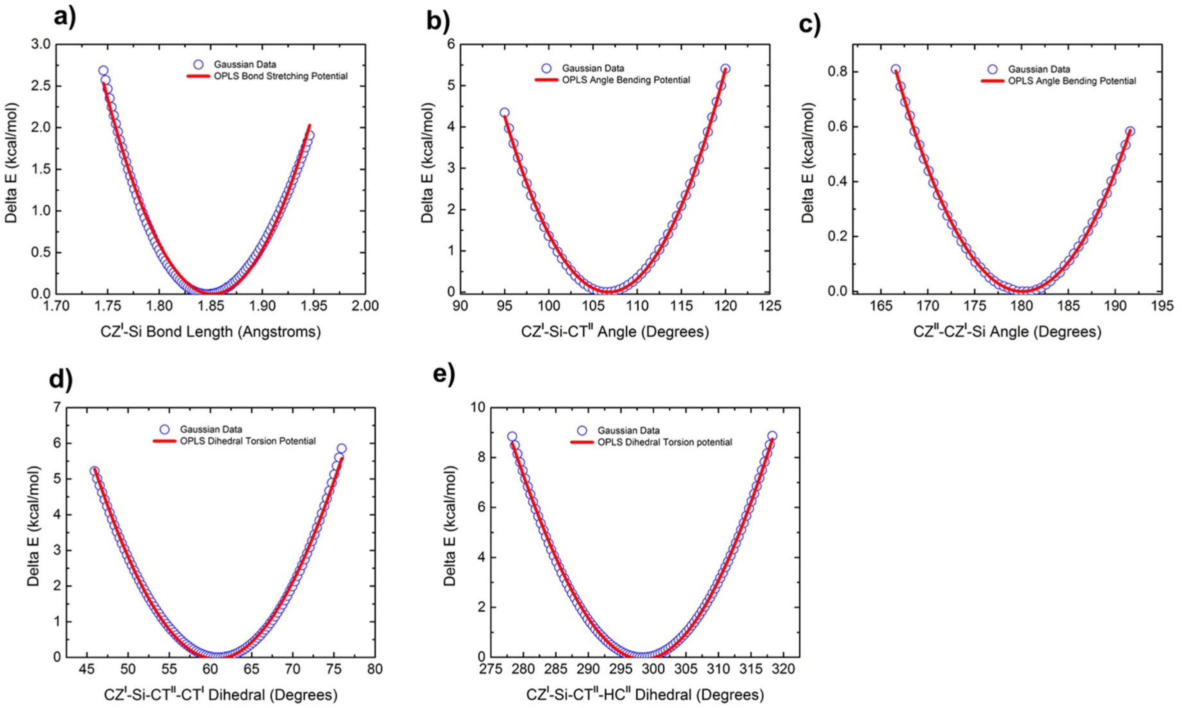

Fig. S33. The comparison between DFT single point energies (blue dots) and the fitted curve (red lines) using the OPLS force field equations for the specific bond length, angle and dihedral angles.

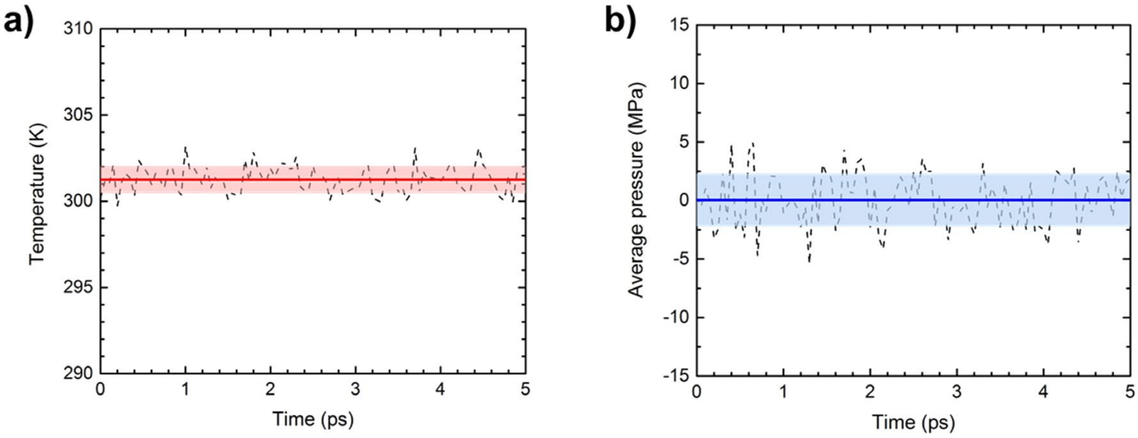

Fig. S34. a The temperature fluctuations and **b** the average pressure fluctuations of the $24 \times 48 \times 1$ supercell model of Form I for the equilibrium 5 ps after running the MD simulation under NPT ensemble at 27°C and zero pressure for 200 ps.

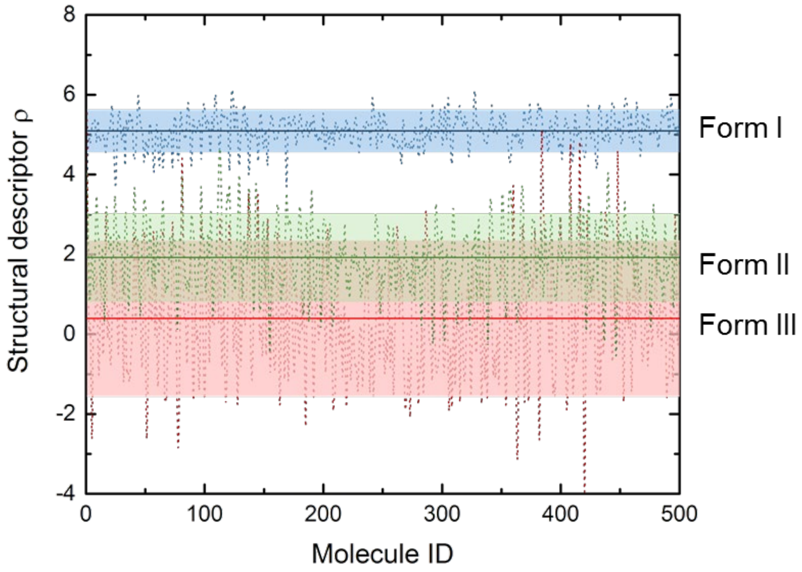

Fig. S35. The value of structural descriptor ρ of each molecule in the 24×24×1 superlattice of three polymorphs at the equilibrium states of MD simulation in the canonical NVT ensemble at 27°C. Each solid line represents the mean value of all calculated structural descriptors (black dots) with the standard deviation shown in the shaded area for each polymorph.

Table S1. The six lattice parameters of three polymorphs in the shear stress-induced SE1 (left panel) and SE2 (right panel) agree well with the experimental data. The percentage differences between simulation and experimental data are shown in the parentheses.

	a	b	c	α	β	γ
Form II	7.58	8.49	17.84	75.9	88.7	70.8
	(–0.3%)	(–1.0%)	(+3.5%)	(–2.9%)	(+2.3%)	(–1.8%)
↓	Shear loading					
Form I	7.53	7.90	16.84	74.1	87.0	79.6
	(-3.0%)	(+2.1%)	(-0.6%)	(-4.9%)	(-1.7%)	(-3.2%)
↓	Unloading					
Form II	7.58	8.44	17.92	75.8	87.2	71.3
	(-0.3%)	(-1.6%)	(-4.0%)	(-3.1%)	(+0.6%)	(-1.1%)

	a	b	c	α	β	γ
Form III	7.74	9.01	17.14	81.3	86.0	67.6
	(+1.8%)	(+0.2%)	(-0.8%)	(-1.2%)	(-4.3%)	(+3.7%)
↓	Shear loading					
Form II	7.51	8.63	17.21	79.5	86.3	72.0
	(-1.2%)	(+0.6%)	(-0.1%)	(+1.7%)	(-0.5%)	(-0.1%)
↓	Unloading					
Form III	7.74	9.06	17.54	81.2	85.8	66.6
	(+1.8%)	(+0.8%)	(+1.5%)	(-1.3%)	(-4.5%)	(+2.2%)

Table S2. Summarized mobility values for single crystal devices (Form I), extracted from Type-1 electrical measurement.

Device ID		**ε = 0%**	**ε = 1.3%**	**ε = 1.9%**	**ε = 2.1%**	**ε = 2.5%**	**ε = 2.8%**	**ε = 3.0%**
Type-1 Device 1	Mobility [cm2V^{-1}]	5.00×10^{-3}	–	5.00×10^{-3}	5.00×10^{-3}	5.00×10^{-3}	5.00×10^{-3}	5.00×10^{-3}
Type-1 Device 2	Mobility [cm2V^{-1}]	3.82×10^{-3}	3.44×10^{-3}	3.34×10^{-3}	3.34×10^{-3}	3.33×10^{-3}	–	3.33×10^{-3}
Type-1 Device 3	Mobility [cm2V^{-1}]	3.00×10^{-3}	2.86×10^{-3}	2.83×10^{-3}	2.91×10^{-3}	–	2.81×10^{-3}	–

Device ID		**ε = 3.1%**	**ε = 3.2%**	**ε = 3.4%**	**ε = 3.8%**	**ε = 4.1%**	**ε = 4.5%**	**ε = 4.9%**
Type-1 Device 1	Mobility [cm2V^{-1}]	5.09×10^{-3}	5.02×10^{-3}	4.71×10^{-3}	4.47×10^{-3}	4.56×10^{-3}	4.01×10^{-3}	4.01×10^{-3}
Type-1 Device 2	Mobility [cm2V^{-1}]	–	3.38×10^{-3}	–	3.06×10^{-3}	3.10×10^{-3}	2.52×10^{-3}	–
Type-1 Device 3	Mobility [cm2V^{-1}]	2.74×10^{-3}	–	2.57×10^{-3}	2.75×10^{-3}	2.45×10^{-3}	1.93×10^{-3}	1.70×10^{-3}

Device ID		**ε = 5.8%**	**ε = 6.4%**	**ε = 6.8%**	**ε = 7.6%**	**ε = 8.5%**	**ε = 9.3%**	**ε = 13.0%**
Type-1 Device 1	Mobility [cm2V^{-1}]	2.61×10^{-3}	2.63×10^{-3}	2.49×10^{-3}	2.29×10^{-3}	–	–	–
Type-1 Device 2	Mobility [cm2V^{-1}]	2.16×10^{-3}	1.50×10^{-3}	0.96×10^{-3}	–	–	–	–
Type-1 Device 3	Mobility [cm2V^{-1}]	–	1.87×10^{-3}	–	1.58×10^{-3}	1.62×10^{-3}	1.60×10^{-3}	1.29×10^{-3}

Channel Dimensions: **T1D1** (L: 178.4 μm, W: 26.6 μm, t: 2.9 μm); **T1D2** (L: 420.9 μm, W: 87.5 μm, t: 3.7 μm); **T1D3** (L: 216.9 μm, W: 53.2 μm, t: 4.0 μm). The thicknesses were characterized based on surface profilometer study. Charge density: 7.61×10^{15} cm^{-3}.[60]

Table S3. Summarized mobility values for single crystal devices (Form Ib), extracted from Type-1 electrical measurement.

Device ID		**ε = 0%**	**ε = 0.8%**	**ε = 1.4%**	**ε = 1.8%**	**ε = 2.1%**	**ε = 2.3%**	**ε = 2.7%**
Type-1 Device 1	Mobility [cm2V^{-1}]	1.54×10^{-3}	1.49×10^{-3}	1.50×10^{-3}	1.51×10^{-3}	1.52×10^{-3}	1.54×10^{-3}	1.55×10^{-3}
Type-1 Device 2	Mobility [cm2V^{-1}]	2.82×10^{-3}	2.59×10^{-3}	2.64×10^{-3}	2.69×10^{-3}	2.74×10^{-3}	2.71×10^{-3}	2.76×10^{-3}
Type-1 Device 3	Mobility [cm2V^{-1}]	1.89×10^{-3}	1.87×10^{-3}	1.87×10^{-3}	1.83×10^{-3}	1.80×10^{-3}	1.80×10^{-3}	1.77×10^{-3}

Device ID		**ε = 3.3%**	**ε = 4.2%**	**ε = 5.0%**	**ε = 6.1%**	**ε = 8.5%**	**ε = 10.6%**	**ε = 13.5%**
Type-1 Device 1	Mobility [cm2V^{-1}]	1.54×10^{-3}	1.54×10^{-3}	1.53×10^{-3}	1.46×10^{-3}	1.38×10^{-3}	1.25×10^{-3}	1.19×10^{-3}
Type-1 Device 2	Mobility [cm2V^{-1}]	2.76×10^{-3}	2.83×10^{-3}	2.77×10^{-3}	2.77×10^{-3}	2.77×10^{-3}	2.62×10^{-3}	2.13×10^{-3}
Type-1 Device 3	Mobility [cm2V^{-1}]	1.78×10^{-3}	1.80×10^{-3}	1.75×10^{-3}	1.77×10^{-3}	1.64×10^{-3}	1.57×10^{-3}	1.42×10^{-3}

Channel Dimensions: **T1D1** (L: 547.62 μm, W: 131.35 μm, t: 13.6 μm); **T1D2** (L: 459.87 μm, W: 75.72 μm, t: 10.7 μm); **T1D3** (L: 518.76 μm, W: 130.03 μm, t: 17.9 μm). The thicknesses were characterized based on surface profilometer study. Charge density: 7.61×10^{15} cm^{-3}.[60]

Table S4. Summarized mobility values for single crystal devices (Form I), extracted from Type-2 electrical measurement.

Device ID		**Cycle 1 (flat)**	**Cycle 1 (bent)**	**Cycle 2 (flat)**	**Cycle 2 (bent)**	**Cycle 3 (flat)**
Type-2 Device 1	Mobility [cm2V^{-1}]	1.63×10^{-3}	1.49×10^{-3}	1.57×10^{-3}	1.49×10^{-3}	1.65×10^{-3}
Type-2 Device 2	Mobility [cm2V^{-1}]	1.00×10^{-3}	1.05×10^{-3}	1.07×10^{-3}	1.06×10^{-3}	1.07×10^{-3}
Type-2 Device 3	Mobility [cm2V^{-1}]	7.34×10^{-3}	7.40×10^{-3}	7.96×10^{-3}	6.96×10^{-3}	7.25×10^{-3}

Device ID		**Cycle 3 (bent)**	**Cycle 4 (flat)**	**Cycle 4 (bent)**	**Cycle 5 (flat)**	**Cycle 5 (bent)**
Type-2 Device 1	Mobility [cm2V^{-1}]	1.59×10^{-3}	1.59×10^{-3}	1.49×10^{-3}	1.54×10^{-3}	1.52×10^{-3}
Type-2 Device 2	Mobility [cm2V^{-1}]	1.06×10^{-3}	1.10×10^{-3}	0.99×10^{-3}	1.09×10^{-3}	1.00×10^{-3}
Type-2 Device 3	Mobility [cm2V^{-1}]	6.86×10^{-3}	7.24×10^{-3}	6.87×10^{-3}	7.15×10^{-3}	6.80×10^{-3}

Channel Dimensions: **T2D1** (L: 178.4 μm, W: 53.5 μm, t: 4.7 μm); **T2D2** (L: 181.0 μm, W: 132.4 μm, t: 3.1 μm); **T2D3** (L: 197.7 μm, W: 50.1 μm, t: 3.2 μm). The thicknesses were characterized based on surface profilometer study. Charge density: 7.61×10^{15} cm^{-3}.[60]

Table S5. The six lattice parameters (a, b, c, α, β, γ) of optimized polymorphs obtained from the structural searching algorithms agree well with the experimental data. The percentage differences between simulation and experimental data are shown in the parentheses.

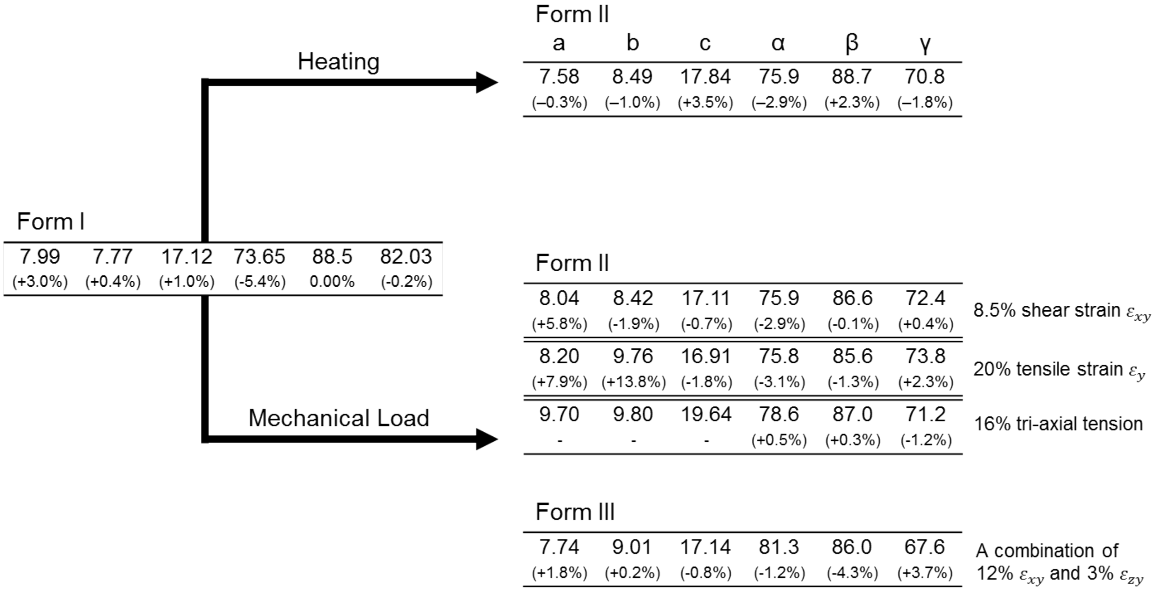

Form I

a	b	c	α	β	γ
7.99 (+3.0%)	7.77 (+0.4%)	17.12 (+1.0%)	73.65 (-5.4%)	88.5 0.00%	82.03 (-0.2%)

Form II

a	b	c	α	β	γ
7.58 (–0.3%)	8.49 (–1.0%)	17.84 (+3.5%)	75.9 (–2.9%)	88.7 (+2.3%)	70.8 (–1.8%)

Form II

a	b	c	α	β	γ	
8.04 (+5.8%)	8.42 (-1.9%)	17.11 (-0.7%)	75.9 (-2.9%)	86.6 (-0.1%)	72.4 (+0.4%)	8.5% shear strain ε_{xy}
8.20 (+7.9%)	9.76 (+13.8%)	16.91 (-1.8%)	75.8 (-3.1%)	85.6 (-1.3%)	73.8 (+2.3%)	20% tensile strain ε_{y}
9.70 -	9.80 -	19.64 -	78.6 (+0.5%)	87.0 (+0.3%)	71.2 (-1.2%)	16% tri-axial tension

Form III

a	b	c	α	β	γ	
7.74 (+1.8%)	9.01 (+0.2%)	17.14 (-0.8%)	81.3 (-1.2%)	86.0 (-4.3%)	67.6 (+3.7%)	A combination of 12% ε_{xy} and 3% ε_{zy}

Table S6. The atom symbol, atomic charges and atom type used in OPLS-AA force field.

Atom symbol	Atomic charge (e)	Atom type in OPLS-AA
CT$^{\mathrm{I}}$	-0.40	Alkane CH3-
CT$^{\mathrm{II}}$	0.35	Alkyl Silane R2CH-Si
CZ$^{\mathrm{I}}$	-0.68	Alkyne RCCR
CZ$^{\mathrm{II}}$	0.38	
CA	-0.09	Aromatic C
HA	0.16	Aromatic H-C
HC$^{\mathrm{I}}$	0.08	Alkane H-C
HC$^{\mathrm{II}}$	-0.06	
Si	0.42	Alkyl Silane R4Si

Table S7. Re-parameterized force field parameters for the bond lengths and angles associated with *sp* carbon atom and silicon atom in TIPS-P molecule.

Bond	K_r $(kcal/(mol \cdot \text{Å}^2))$	l_0 (Å)
CZ$^{\mathrm{I}}$-Si	227.5168	1.8516
Angle	K_θ $(kcal/(mol \cdot rad^2))$	θ_0 (°)
CZ$^{\mathrm{I}}$-Si-CT$^{\mathrm{II}}$	101.1104	106.7551
CZ$^{\mathrm{II}}$-CZ$^{\mathrm{I}}$-Si	14.4443	180.0790

Table S8. Re-parameterized force field parameters for the dihedral angles associated with *sp* carbon atom and silicon atom in TIPS-P molecule.

Dihedral	V_1 $(kcal/mol)$	V_2 $(kcal/mol)$	V_3 $(kcal/mol)$
CZ$^{\mathrm{I}}$-Si-CT$^{\mathrm{II}}$-CT$^{\mathrm{I}}$	1.5198	-1.5644	37.1337
CZ$^{\mathrm{I}}$-Si-CT$^{\mathrm{II}}$-HC$^{\mathrm{II}}$	3.3464	-3.3793	34.4374

Movie S1.
Thermoelasticity of TIPS-P crystal. Heating and cooling rates are 10°C min^{-1}.

Movie S2.
Superelasticity (SE1) in Form II crystal. $[\bar{1}00]$-shearing using a micromanipulator tip is carried out at 150°C.

Movie S3.
Superelasticity (SE2) in Form III crystal. $[\bar{1}00]$-shearing using a micromanipulator tip is carried out at 220°C.

Movie S4.
Ferroelasticity (FE1) in Form I(b) crystal. $[100]$-shearing using a micromanipulator tip is carried out at 100°C.

Movie S5.
Ferroelasticity (FE1) in Form II crystal. $[100]$-shearing using a micromanipulator tip is carried out at 150°C.

Movie S6.
MD simulated FE1 in Form I structure.

Movie S7.
Ferroelasticity (FE2) in Form I crystal. $[010]$-tension and compression is carried out by bending crystal on a PET substrate.

Movie S8.
MD simulated FE2 in Form I structure.

Supporting Structure 1. (separate file)
Preliminary structure of Form III phase of TIPS-P crystal.

Supporting Structure 2. (separate file)
Single crystal X-ray structure of twinned Form I.

References:

46. Gaussian 09, M. J. Frisch, G. W. Trucks, H. B. Schlegel, G. E. Scuseria, M. A. Robb, J. R. Cheeseman, G. Scalmani, V. Barone, B. Mennucci, G. A. Petersson, H. Nakatsuji, M. Caricato, X. Li, H. P. Hratchian, A. F. Izmaylov, J. Bloino, G. Zheng, J. L. Sonnenberg, M. Hada, M. Ehara, K. Toyota, R. Fukuda, J. Hasegawa, M. Ishida, T. Nakajima, Y. Honda, O. Kitao, H. Nakai, T. Vreven, J. J. A. Montgomery, J. E. Peralta, F. Ogliaro, M. Bearpark, J. J. Heyd, E. Brothers, K. N. Kudin, V. N. Staroverov, R. Kobayashi, J. Normand, K. Raghavachari, A. Rendell, J. C. Burant, S. S. Iyengar, J. Tomasi, M. Cossi, N. Rega, J. M. Millam, M. Klene, J. E. Knox, J. B. Cross, V. Bakken, C. Adamo, J. Jaramillo, R. Gomperts, R. E. Stratmann, O. Yazyev, A. J. Austin, R. Cammi, C. Pomelli, J. W. Ochterski, R. L. Martin, K. Morokuma, V. G. Zakrzewski, G. A. Voth, P. Salvador, J. J. Dannenberg, S. Dapprich, A. D. Daniels, Ö. Farkas, J. B. Foresman, J. V. Ortiz, J. Cioslowski, D. J. Fox (Gaussian, Inc., Wallingford, CT, 2009).
47. G. Kresse, J. Furthmüller, *Phys. Rev. B* **1996**, *54*, 11169.
48. S. Grimme, J. Antony, S. Ehrlich, H. Krieg, *J. Chem. Phys.* **2010**, *132*, 154104.
49. J. P. Perdew, K. Burke, M. Ernzerhof, *Phys. Rev. Lett.* 1996, **77**, 3865.
50. J. Hutter, M. Iannuzzi, F. Schiffmann, J. VandeVondele, *Wiley Interdiscip. Rev. Comput. Mol. Sci.* **2014**, *4*, 15-25.
51. J. VandeVondele, J. Hutter, *J. Chem. Phys.* **2007**, *127*, 114105.
52. J. VandeVondele, M. Krack, F. Mohamed, M. Parrinello, T. Chassaing, J. Hutter, *Comput. Phys. Commun.* **2005**, *167*, 103-128.
53. M. Krack, *Theor. Chem. Acc.* **2005**, *114*, 145-152.
54. S. Plimpton, *J. Comput. Phys.* **1995**, *117*, 1-19.
55. W. L. Jorgensen, D. S. Maxwell, J. Tirado-Rives, *J. Am. Chem. Soc.* **1996**, *118*, 11225-11236.
56. M. A. Meyers, K. K. Chawla, *Mechanical behavior of materials*, Cambridge university press, New York, **2008**.
57. G. J. Martyna, D. J. Tobias, M. L. Klein, *J. Chem. Phys.* **1994**, *101*, 4177-4189.
58. E. E. Santiso, B. L. Trout, *J. Chem. Phys.* **2011**, *134*, 064109.
59. J. E. Anthony, *Angew. Chem. Int. Ed.* **2008**, *47*, 452-483.
60. K. S. Park, K. S. Lee, C.-M. Kang, J. Baek, K. S. Han, C. Lee, Y.-E. K. Lee, Y. Kang, M. M. Sung, *Nano Lett.* **2015**, *15*, 289-293.